The Astrophysical Journal, 941:100 (28pp), 2022 December 10 https://doi.org/10.3847/1538-4357/ac8d04

"Super-kilonovae" from Massive Collapsars as Signatures of Black Hole Birth in the Pair-instability Mass Gap

Daniel M. Siegel[1,2,3], Aman Agarwal[1,2,3], Jennifer Barnes[4,5], Brian D. Metzger[4,6], Mathieu Renzo[4,6], and V. Ashley Villar[4,6,7,8,9]

[1] Perimeter Institute for Theoretical Physics, Waterloo, Ontario, N2L 2Y5, Canada
[2] Department of Physics, University of Guelph, Guelph, Ontario, N1G 2W1, Canada
[3] Institute of Physics, University of Greifswald, D-17489 Greifswald, Germany
[4] Columbia Astrophysics Laboratory, Columbia University, New York, NY 10027, USA
[5] Kavli Institute for Theoretical Physics, University of California, Santa Barbara, CA 93106, USA
[6] Center for Computational Astrophysics, Flatiron Institute, New York, NY 10010, USA
[7] Department of Astronomy & Astrophysics, The Pennsylvania State University, University Park, PA 16802, USA
[8] Institute for Computational & Data Sciences, The Pennsylvania State University, University Park, PA 16802, USA
[9] Institute for Gravitation and the Cosmos, The Pennsylvania State University, University Park, PA 16802, USA
Received 2021 November 4; revised 2022 August 13; accepted 2022 August 21; published 2022 December 14

Abstract

The core collapse of rapidly rotating massive $\sim 10M_{\odot}$ stars ("collapsars"), and the resulting formation of hyperaccreting black holes, comprise a leading model for the central engines of long-duration gamma-ray bursts (GRBs) and promising sources of *r*-process nucleosynthesis. Here, we explore the signatures of collapsars from progenitors with helium cores $\gtrsim 130M_{\odot}$ above the pair-instability mass gap. While the rapid collapse to a black hole likely precludes prompt explosions in these systems, we demonstrate that disk outflows can generate a large quantity (up to $\gtrsim 50M_{\odot}$) of ejecta, comprised of $\gtrsim 5$–$10M_{\odot}$ in *r*-process elements and ~ 0.1–$1M_{\odot}$ of ^{56}Ni, expanding at velocities ~ 0.1 c. Radioactive heating of the disk wind ejecta powers an optical/IR transient, with a characteristic luminosity $\sim 10^{42}$ erg s^{-1} and a spectral peak in the near-IR (due to the high optical/UV opacities of lanthanide elements), similar to kilonovae from neutron star mergers, but with longer durations $\gtrsim 1$ month. These "super-kilonovae" (superKNe) herald the birth of massive black holes $\gtrsim 60M_{\odot}$, which—as a result of disk wind mass loss—can populate the pair-instability mass gap "from above," and could potentially create the binary components of GW190521. SuperKNe could be discovered via wide-field surveys, such as those planned with the Roman Space Telescope, or via late-time IR follow-up observations of extremely energetic GRBs. Multiband gravitational waves of ~ 0.1–50 Hz from nonaxisymmetric instabilities in self-gravitating massive collapsar disks are potentially detectable by proposed observatories out to hundreds of Mpc; in contrast to the "chirp" from binary mergers, the collapsar gravitational-wave signal decreases in frequency as the disk radius grows ("sad trombone").

Unified Astronomy Thesaurus concepts: Astrophysical black holes (98); Stellar mass black holes (1611); High energy astrophysics (739); Gravitational waves (678); Gravitational wave sources (677); Late stellar evolution (911); Stellar evolution (1599); Gamma-ray bursts (629); Core-collapse supernovae (304); Gravitational collapse (662); Transient sources (1851); Time domain astronomy (2109)

1. Introduction

The astrophysical locations that give rise to the synthesis of heavy nuclei via the rapid capture of neutrons onto lighter seed nuclei (the *r*-process; Burbidge et al. 1957; Cameron 1957) remain a topic of active debate (see Horowitz et al. 2019; Cowan et al. 2021; Siegel 2022 for recent reviews). Several lines of evidence, ranging from measurements of radioactive isotopes on the sea floor (e.g., Hotokezaka et al. 2015; Wallner et al. 2015) to the abundances of metal-poor stars formed in the smallest dwarf galaxies (e.g., Ji et al. 2016; Tsujimoto et al. 2017), suggest that the dominant sites of the *r*-process are much rarer than ordinary core-collapse supernovae (CCSNe), both in the early history of our Galaxy and today. The most promising contenders are mergers of neutron star binaries (e.g., Lattimer & Schramm 1974; Symbalisty & Schramm 1982) and rare channels of CCSNe, such as those that give birth to a rapidly spinning magnetar (Thompson et al. 2004; Metzger et al. 2007; Winteler et al. 2012; Nishimura et al. 2015) or a hyperaccreting black hole ("collapsar"; e.g., Surman et al. 2008; Siegel et al. 2019; see also Grichener & Soker 2019). Perhaps not coincidentally, these two types of events —neutron star mergers and collapsars—are the leading models for the central engines of gamma-ray bursts (GRBs) of the short- and long-duration classes, respectively (e.g., Woosley & Bloom 2006; Berger 2014).

The radioactive decay of *r*-process elements in the ejecta of a neutron star merger powers a short-lived optical/IR transient known as a kilonova (Li & Paczyński 1998; Metzger et al. 2010; Barnes & Kasen 2013). However, the large quantity of *r*-process ejecta $\gtrsim 0.02$–$0.06M_{\odot}$ inferred from the kilonova accompanying GW170817, as well as the relatively low inferred outflow velocity ~ 0.1 c of the bulk of this material (e.g., Cowperthwaite et al. 2017; Drout et al. 2017; Villar et al. 2017), do not agree with the predictions from numerical relativity for the mass ejected during the early dynamical phase of the merger (see Metzger 2019; Siegel et al. 2019; Margutti & Chornock 2021; Nakar 2020 for reviews). Instead, the dominant ejecta source in GW170817, and likely in the majority of neutron star mergers, are delayed outflows from the accretion disk that forms around the black hole (BH) or neutron

star remnant (e.g., Metzger et al. 2008; Fernández & Metzger 2013; Just et al. 2015; Siegel & Metzger 2017, 2018; Fujibayashi et al. 2018). General relativistic magnetohydrodynamical (GRMHD) simulations of the long-term evolution of postmerger disks find that up to ∼30% of the original mass is unbound in outflows with average velocities ∼0.1 c (Siegel & Metzger 2017; Fujibayashi et al. 2018, 2020; Christie et al. 2019; Fernández et al. 2019), broadly consistent with the kilonova observed from GW170817.

As emphasized by Siegel et al. (2019), similar accretion disk outflows to those generated in neutron star mergers also occur in collapsars (see also MacFadyen & Woosley 1999; Janiuk et al. 2004; Surman et al. 2006; Miller et al. 2020; Just et al. 2022). Unlike in the merger case, the collapsing stellar material feeding the disk is composed of roughly equal numbers of protons and neutrons (electron fraction $Y_e \simeq 0.5$). However, for mass accretion rates above a critical threshold value ($\gtrsim 10^{-1}$–$10^{-3} M_\odot$ s^{-1}, which depends on the effective viscosity and BH mass; Chen & Beloborodov 2007; Metzger et al. 2008), the inner regions of the disk are electron-degenerate and "self-neutronize" via electron captures on protons (e.g., Beloborodov 2003), thus maintaining a low electron fraction $Y_e \approx 0.1$ in a regulated process (Siegel & Metzger 2017). As a result, the collapsar disk outflows, which feed on this neutron-rich reservoir, can themselves possess a sufficiently high neutron concentration to enable an *r*-process, during much of the epoch in which the GRB jet is being powered. However, the details of the synthesized composition—particularly the partitioning between light and heavy *r*-process elements—are sensitive to the impact of neutrino absorption processes on the electron fraction of the outflowing material (Surman et al. 2006; Miller et al. 2020; Li & Siegel 2021).

In comparison to neutron star mergers, collapsars hold several complementary advantages as *r*-process sources (Siegel et al. 2019). First, as a result of being promptly generated from very massive stars, and being empirically found to occur in small dwarf galaxies at low metallicity (e.g., Fruchter et al. 2006), collapsars naturally explain the *r*-process enrichment in ultra-faint dwarf galaxies, such as Reticulum II (e.g., Ji et al. 2016), and metal-poor stars in the Galactic halo (e.g., Brauer et al. 2021). Furthermore, if the gamma-ray luminosity of GRBs scales with the BH accretion rate in the same way in mergers as in collapsars, then, from the relative rate and gamma-ray fluence distributions of long- versus short-duration GRBs, one is led to conclude that the total mass accreted via collapsar disks over cosmic time (and hence the integrated amount of disk wind ejecta) could exceed that of neutron star mergers (Siegel et al. 2019). Arguments based on the chemical evolution history of the early Milky Way galaxy have been made in favor of both rare SNe/collapsars (Côté et al. 2019; Siegel et al. 2019; van de Voort et al. 2020; Yamazaki et al. 2021; Brauer et al. 2021) and mergers (Shen et al. 2015; Duggan et al. 2018; Bartos & Márka 2019; Holmbeck et al. 2019; Macias & Ramirez-Ruiz 2019; Tarumi et al. 2021) as early *r*-process sources.

While the kilonova from GW170817 provided ample evidence that neutron star mergers can execute an *r*-process, the same signature has not yet been seen from the SNe observed in coincidence with long GRBs. However, this fact is not necessarily constraining at the moment, due to *r*-process material being easier to hide in the collapsar case. In particular, a prompt and powerful SN explosion may be required to explain the large masses of ^{56}Ni inferred from GRB SN light curves (e.g., Cano 2016; Barnes et al. 2018; however, see also Zenati et al. 2020). By contrast, the *r*-process-generating disk outflows occur over longer times, up to tens of seconds or more after collapse, commensurate with the observed duration of long GRBs. Unless they are efficiently mixed to the highest velocities, the *r*-process elements (and any associated photometric or spectroscopic signatures) are therefore buried behind several solar masses of "ordinary" SN ejecta (dominated by α-elements, such as oxygen).

Nevertheless, if they are present in the inner ejecta layers, *r*-process elements could manifest as a late-time IR signal (Siegel et al. 2019) arising from the high opacity of heavy *r*-process nuclei (Kasen et al. 2013; Tanaka & Hotokezaka 2013). This signal is challenging to detect, given the typically large distances to GRB SNe and the late times required (at which point the emission is faint). The detection prospects will improve with the advent of the James Webb Space Telescope (JWST), particularly if the nebular spectra of lanthanide-rich material also peaks in the IR (Hotokezaka et al. 2021).

Collapsars of the type that have been observed as SNe so far may also only represent a subset of accretion-powered CC events. The progenitor stars that give rise to long GRBs are typically believed to possess zer0-age main sequence (ZAMS) masses $\lesssim 40 M_\odot$, with helium cores at death of $\lesssim 10 M_\odot$ (e.g., Woosley & Heger 2006). Upon the collapse of their iron cores, these events first go through a rapidly rotating proto–neutron star phase (Dessart et al. 2008), in which a millisecond magnetar is formed (Thompson & Duncan 1993; Raynaud et al. 2020). The strong and collimated outflow from such a magnetar during the first seconds after its birth (Thompson et al. 2004; Metzger et al. 2007), before it accretes sufficient matter to collapse into a BH, may play an important role in shock heating and in unbinding many of the outer layers of the star and generating the required large ^{56}Ni masses (e.g., Shankar et al. 2021).

On the other hand, the number of long GRBs with detected SNe only number around a dozen, and the majority of these are associated with the volumetrically more common, but physically distinct, "low luminosity" class of GRBs (e.g., Liang et al. 2007). It thus remains unclear whether the more energetic classical long GRBs always occur in coincidence with ^{56}Ni-powered SNe. Indeed, luminous SNe have been ruled out for a few nominally long GRBs (e.g., Fynbo et al. 2006; Gehrels et al. 2006; Rastinejad et al. 2022), although the nature of these events (e.g., whether they are actually short GRBs masquerading as collapsars) remains unclear (e.g., Zhang et al. 2007).

Within this context, we consider in this paper the fate of stars that are initially much more massive, those with ZAMS masses $M_{\rm ZAMS} \gtrsim 260 M_\odot$, which are predicted to evolve helium cores by the time of CC above the pair-instability (PI) gap $\gtrsim 130 M_\odot$ (e.g., Woosley et al. 2002; Woosley 2017; Farmer et al. 2020; Renzo et al. 2020b; Woosley & Heger 2021). If the initial mass function (IMF) is an indication, such stars are potentially much rarer than the ordinarily considered collapsar progenitors with $M_{\rm ZAMS} \lesssim 40 M_\odot$. On the other hand, if such stars are rapidly spinning (e.g., Marchant et al. 2019; Marchant & Moriya 2020)—possibly because of continuous gas accretion throughout their lifetime (e.g., Cantiello et al. 2021; Jermyn et al. 2021; Dittmann et al. 2021)—and if they form collapsar-like disks upon collapse in proportion to their (much higher) helium core

masses, their resulting yields of *r*-process ejecta in disk winds could be substantially greater.

Another key difference is that a prompt explosion (e.g., as attributed to a protomagnetar above, or fallback accretion; Powell et al. 2021) is more challenging to obtain for these very massive stars. This is because (1) the nominal timescale for BH formation is much faster, within $\lesssim$0.1 s, due to large masses exceeding $2M_\odot$ and the great compactness of their iron cores (e.g., Renzo et al. 2020b), and (2) their larger $\gtrsim 10^{53}$ erg gravitational binding energies, relative to those of lower-mass helium cores $\lesssim 10^{52}$ erg, exceed the rotational energies of even maximally spinning neutron stars. As a result of the assuredly failed initial explosions of post-PI cores, these systems are unlikely to eject a large quantity of prompt, shock-synthesized ^{56}Ni and unprocessed stellar material (however, see Fujibayashi et al. 2021). Instead, the bulk of the ejecta will arise over longer timescales, from disk outflows, which—scaling up from low-mass collapsars—could amount to $\gtrsim 10M_\odot$ of *r*-process and Fe-group elements (including ^{56}Ni).

Rather than the usual picture of GRB SNe, the type of collapse transient above the PI gap that we envision is in some ways more akin to a scaled-up neutron star merger. At risk of committing etymological heresy, we therefore refer to these massive collapsar transient events as "super-kilonovae" (or superKNe). As we discuss, if superKNe exist, their long durations and red colors may render them potentially identifiable either through follow-up IR observations of long GRBs (e.g., with JWST) or blindly, in surveys with the Vera Rubin Observatory (Tyson 2002) or the Nancy Grace Roman Space Telescope (Roman; Spergel et al. 2015).

The gravitational-wave observatory LIGO/Virgo detected a binary BH merger, GW190521, for which both binary components—of masses $\sim 85M_\odot$ and $\sim 66M_\odot$, respectively (Abbott et al. 2020)—were inside the nominal PI mass gap.[10] Tentative evidence suggests the effective high BH spin of the progenitor binary, albeit with the spin axis being misaligned with the orbital momentum axis (however, see Mandel & Fragos 2020; Nitz & Capano 2021). These unusual properties have motivated a number of theoretical studies proposing new ways to populate the PI mass gap, such as through dynamical stellar mergers (e.g., Di Carlo et al. 2019, 2020; Renzo et al. 2020a), hierarchical BH mergers in dense environments (e.g., Antonini & Rasio 2016; Yang et al. 2019; Gerosa & Fishbach 2021; Tagawa et al. 2021), modifying stellar physics at low metallicity (e.g., Farrell et al. 2021; Vink et al. 2021), or external gas accretion (e.g., Safarzadeh & Haiman 2020). As we describe, if both the BHs acquired their low expected masses and high spin as a result of inefficient disk accretion, superKN events of the type envisioned here provide a novel single-star channel for filling the PI mass gap "from above."

This paper is organized as follows. Section 2 presents a semi-analytic model for the collapse of rotating massive stars, their accretion disks and disk wind ejecta, and the resulting heavy-element nucleosynthesis, which builds on earlier work in Siegel et al. (2019). After calibrating the model so that collapsars generate BH accretion events consistent with the observed properties of long-GRB jets, we then apply it to more massive $\gtrsim 130M_\odot$ progenitors above the PI mass gap. In Section 3, using our results for the disk wind ejecta, we calculate the light curves and spectra of their superKN emission, by means of Monte Carlo radiative transfer simulations. Section 4 explores the prospects for discovering superKNe with future optical/IR surveys or in follow-up observations of long GRBs. Section 5 discusses several implications of our findings, including gravitational-wave emission from the self-gravitating phases of the collapsar disk evolution, the astrophysical origin of GW190521, and the luminous radio and optical emission that results from the superKN ejecta interacting with surrounding gas. Section 6 summarizes our results.

2. Disk Outflow Model

2.1. Stellar Models

To model the precollapse structure of the superKN progenitors, we employ the MESA stellar evolution models of Renzo et al. (2020b), publicly available at 10.5281/zenodo.3406357. The simulations start from naked helium cores of metallicity $Z = 0.001$, which are then self-consistently evolved from helium core ignition, through possible (pulsational) PI (PPI), to the onset of CC (defined as when the radial infall velocity exceeds 1000 km s^{-1}). We label the input stellar models according to their initial helium core mass—e.g., model `200.25` corresponds to $M_{\rm He,init} = 200.25M_\odot$—and focus on models "above" the PI gap, which do not experience PI-driven pulses.

The models are computed using a 22-isotope nuclear reaction network, which is sufficient to capture the bulk of the energy generation throughout the stellar evolution, but cannot accurately capture the weak interactions in the innermost core (e.g., Farmer et al. 2016). However, the deepest layers of the core promptly fall into the newly formed BH (see Section 2.2), and hence they do not contribute to the accretion disk and its outflows.

These models were evolved without rotation, which we instead artificially impose at the point of CC (see Section 2.2). The main effect of rotation during the pre-CC evolution is mixing at the core–envelope interface, which leads to more massive helium cores for a given initial mass. In the extreme case of chemically homogeneous evolution (Maeder & Meynet 2000), the entire star may become a helium core. This will impact how many stars develop core masses reaching the PI/PPI regime or beyond, and thus the predicted population statistics. However, because Renzo et al. (2020b) only simulate the helium core, this does not affect our present study. Rotation can also enhance the wind mass-loss rate (e.g., Langer 1998), and increase the radius in the outer layers at the rotational equator by up to 50%, which is neglected in the progenitors that we use. Finally, by adding centrifugal support to the core, rotation can modestly increase the PI/PPI mass range (e.g., Glatzel et al. 1985).[11]

For sufficiently large initial core masses $M_{\rm He,init} \gtrsim 200\,M_\odot$, the final mass at collapse would nominally produce a BH above the PI mass gap—neglecting the subsequent mass loss in the accretion disk outflows, as explored in the present study. This

[10] However, see Fishbach & Holz (2020) and Nitz & Capano (2021), who interpret GW190521 as a merger between one BH below the PI gap and one above.

[11] For example, using a setup similar to that of Renzo et al. (2020b), Marchant & Moriya (2020) study the impact of an initial rotation frequency $\omega/\omega_{\rm crit} = 0.9$, where $\omega_{\rm crit} \equiv \sqrt{(1 - L_\star/L_{\rm Edd})GM_\star/R_\star^3}$ and $L_\star/L_{\rm Edd}$ is the stellar luminosity in units of Eddington luminosity. They found a $\sim 4\%$ ($\sim 15\%$) increase in the maximum BH mass below the PI mass gap, assuming that angular momentum is transported by a Tayler–Spruit dynamo (assuming no angular momentum transport). The stronger angular momentum coupling found by Fuller & Ma (2019) would likely result in an even more modest effect.

arises because the gravitational energy released by the PI-driven collapse acts to photodisintegrate the nuclei produced in the thermonuclear explosion, instead of generating outward bulk motion (e.g., Bond et al. 1984). Since these models do not experience pulses of mass loss, their precollapse total mass is determined by the assumed wind mass-loss prescription: the minimum final helium core mass above the PI mass gap for our MESA models is $M_{\rm He,fin} \gtrsim 125\,M_\odot$. Renzo et al. (2020b) estimated the corresponding final BH mass (again, neglecting postcollapse disk outflows) as the total baryonic mass with binding energy $> 10^{48}$ ergs, which effectively corresponds to the total final mass within a few $0.1\,M_\odot$ (e.g., Farmer et al. 2019; Renzo et al. 2020b).

A key ingredient in modeling fallback accretion is the radial density profile of the star at collapse (Section 2.2). Despite their large masses, helium stars above the PI gap remain compact throughout their lifetimes, never expanding as a result of PI pulses. Their typical radii $R_\star \approx 10\,R_\odot$ are similar to those of the normally considered Wolf–Rayet progenitors of GRBs (e.g., Woosley & Heger 2006; Figure 1). If stars in this mass range reach CC with their hydrogen envelope intact (e.g., for sufficiently low metallicity, as in Population III stars), their radii could be considerably larger; however, no red supergiants of this mass have yet been observed.

We also employ the $15\,M_\odot$ and $20\,M_\odot$ single-star (hydrogen-rich) models from Heger et al. (2000), to test our collapsar model on more canonical long-GRB progenitors (see Appendix E for a discussion of the results). These are computed as starting from a surface equatorial velocity of $200\,{\rm km\,s^{-1}}$ at ZAMS, and they assume that the mean molecular weight gradients do not impede rotational mixing ($f_\mu = 0$; "weak molecular weight barriers"). They are labeled E15 and E20, respectively, and are publicly available at https://2sn.org/stellarevolution/rotation/.

2.2. Collapsar Model

The masses and composition of the superKNe ejecta are computed by modeling the collapse of a progenitor star. Depending on the stellar angular momentum profile, the collapse and fallback of the envelope material leads to the formation of an accretion disk, which gives rise to massive neutron-rich disk outflows (Siegel et al. 2019; Miller et al. 2020; Just et al. 2022). Although the rotation profiles of massive stars at the time of CC—particularly those above the PI mass gap considered here—are highly uncertain (e.g., Heger et al. 2000; Ma & Fuller 2019; Marchant & Moriya 2020), the specific angular momentum j_z generally increases with stellar radius. Infalling stellar material thus circularizes at increasingly larger radii from the BH with time.

We endow the stellar models with mass $M_\star$ and radius $R_\star = R_{\rm He,fin}$ at the time of CC (Section 2.1 with an angular momentum profile that assumes rigid rotation on spherical shells, with angular velocity $\Omega(r,\,\theta) = \Omega(r)$. This results in

$$j_z(r,\,\theta) = j(r)\sin^2(\theta), \tag{1}$$

where r, θ are the radial and polar angle coordinates, respectively. We adopt a general parameterized angular momentum profile of the form

$$j(r) = \begin{cases} f_{\rm K} j_{\rm K}(r)\left(\dfrac{r}{r_{\rm b}}\right)^p, & r < r_{\rm b} \\ f_{\rm K} j_{\rm K}(r), & r_{\rm b} \leqslant r \leqslant R_\star \end{cases}, \tag{2}$$

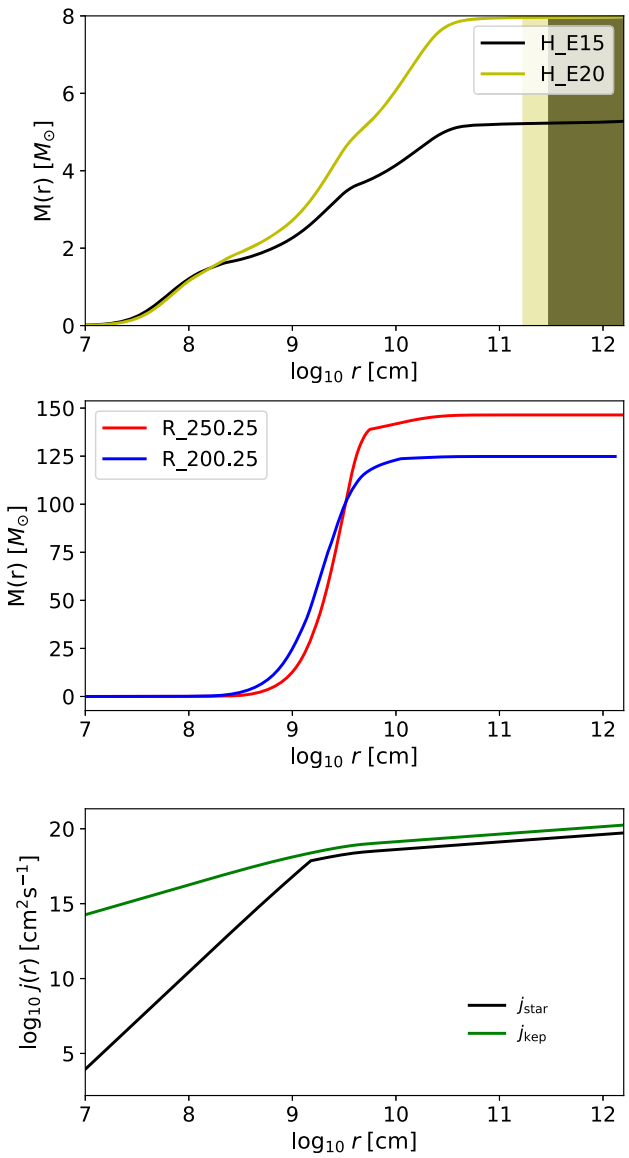

Figure 1. Properties of the stellar models at the onset of collapse, showing the enclosed mass as a function of stellar radius (top: models E15 and E20 of Heger et al. 2000; center: models 200.0 and 250.25 of Renzo et al. 2020b), with an example of the imposed specific angular momentum profile for model 250.25, with $p = 4.5$, $r_{\rm b} = 1.5 \times 10^9$ cm, and $f_{\rm K} = 0.3$ (see Equation (2)), compared to the corresponding Keplerian profile (solid green line; bottom). The light (dark) shaded region in the top panel represents the hydrogen envelope of the E20 (E15) model. Such envelopes are absent from the models of Renzo et al. (2020b).

where $r_{\rm b}$, p, and $f_{\rm K}$ are free parameters. This corresponds to a low-density "envelope," composed primarily of helium in the models considered here, rotating at a fraction $f_{\rm K} < 1$ of the local Keplerian angular momentum $j_{\rm K} = \sqrt{GM_{\rm enc}(r)r}$, where $M_{\rm enc}(r)$ is the mass enclosed interior to the radius r, and an inner "core," in which rotation is suppressed by a power law with index p relative to the fraction of local breakup rotation adopted for the envelope. Although the parameter values ($r_{\rm b}$, p, $f_{\rm K}$) are uncertain, as we discuss below, they can be "calibrated" to produce the timescales and energetics of disk accretion that are consistent with the observed properties of long-GRB jets. Figure 1 illustrates the parameterized rotation profile for model 250.25.

Assuming an axisymmetric rotating star, we discretize the progenitor stellar model into (n_r, n_θ) mass elements, logarithmically spaced in stellar radius r and uniformly spaced in $\cos\theta$. The angular resolution is chosen to be sufficiently high (typically $n_\theta = 1001$) such that the accuracy when numerically computing global quantities by integration (total mass, total fallback mass, etc.) is dominated by the finite radial resolution of the stellar progenitor models. Defining $t = 0$ as the onset of CC, a given stellar layer at radius r will start to collapse onto the center at the sound travel time $t_s(r) = \int_0^r c_s^{-1}(r)\mathrm{d}r$ from the center to r. Due to its finite angular momentum, a given fluid element will do so on an eccentric trajectory and circularize on the equatorial plane at the time (see Kumar et al. 2008)

$$t_{\rm circ}(r,\,\theta) = t_{\rm s}(r) + \frac{(1+e)^{-3/2}}{\Omega_{\rm K}(r)}[\cos^{-1}(-e) + e(1-e^2)^{1/2}] \quad (3)$$

and radius

$$r_{\rm circ}(r,\,\theta) = \left(\frac{8}{3\pi}\right)^2 r(1-e), \quad (4)$$

where $e(r,\,\theta) = 1 - [\Omega^2(r)/\Omega_{\rm K}^2(r)]\sin^2\theta$ is the eccentricity of the trajectory and $\Omega_{\rm K} = (GM_{\rm enc}(r)/r^3)^{1/2}$ is the Keplerian angular velocity.

The innermost parts of the stellar core may not possess sufficient angular momentum to circularize into an accretion disk, so, instead, they directly collapse into a BH. We define the initial BH as a "seed BH" that is formed by the innermost stellar layers up to radius $r_{\bullet,0}$, with enclosed mass $M_{\bullet,0} = 0.5\,M_\odot$, a safe assumption for all the stellar models considered here. This seed BH has the dimensionless spin parameter

$$a_{\bullet,0} = \frac{cJ_{\rm enc}(r_{\bullet,0})}{GM_{\rm enc}^2(r_{\bullet,0})}, \quad (5)$$

where $J_{\rm enc}(r)$ is the enclosed angular momentum, G is the gravitational constant, and c is the speed of light. The corresponding innermost stable circular orbit (ISCO) is given by Bardeen et al. (1972):

$$r_{\rm ISCO}(M_\bullet,\,a_\bullet) = \frac{GM_\bullet}{c^2} \times \{3 + z_2 - [(3-z_1)(3+z_1+2z_2)]^{1/2}\}, \quad (6)$$

where

$$z_1 = 1 + (1-a_\bullet^2)^{1/3}[(1+a_\bullet)^{1/3} + (1-a_\bullet)^{1/3}], \quad (7)$$

$$z_2 = (3a_\bullet^2 + z_1^2)^{1/2}. \quad (8)$$

At the initial BH formation, we follow the collapse of the outer stellar layers, according to Equations (3) and (4), and distinguish between the mass elements that circularize outside the BH to form a disk ($r_{\rm circ}(r(t),\,\theta) > r_{\rm ISCO}(t)$), giving rise to a "disk feeding rate" $\dot{m}_{\rm fb,disk}$, and those that directly fall into the BH without accreting through a disk ($r_{\rm circ}(r(t),\,\theta) \leqslant r_{\rm ISCO}(t)$), giving rise to a direct fallback rate onto the BH $\dot{m}_{\rm fb,\bullet}$. Here, $r(t)$ refers to the radius of a stellar element at polar angle θ that circularizes at time t in the equatorial plane. We denote the associated rates of angular momentum supplied to the disk and the BH with $\dot{J}_{\rm fb,disk}$ and $\dot{J}_{\rm fb,\bullet}$, respectively.

We follow the evolution of the BH, disk, and ejecta properties by solving the following equations:

$$\frac{\mathrm{d}M_\bullet}{\mathrm{d}t} = \dot{m}_{\rm fb,\bullet} + \dot{m}_{\rm acc}, \quad (9)$$

$$\frac{\mathrm{d}J_\bullet}{\mathrm{d}t} = \dot{J}_{\rm fb,\bullet} + \dot{m}_{\rm acc} j_{\rm ISCO}, \quad (10)$$

$$\frac{\mathrm{d}M_{\rm disk}}{\mathrm{d}t} = \dot{m}_{\rm fb,disk} - \dot{m}_{\rm acc} - \dot{m}_{\rm wind}, \quad (11)$$

$$\frac{\mathrm{d}J_{\rm disk}}{\mathrm{d}t} = \dot{J}_{\rm fb,disk} - \dot{m}_{\rm acc} j_{\rm ISCO} - \dot{J}_{\rm wind}, \quad (12)$$

$$\frac{\mathrm{d}M_{\rm ejecta}}{\mathrm{d}t} = \dot{m}_{\rm wind}, \quad (13)$$

$$\frac{\mathrm{d}J_{\rm ejecta}}{\mathrm{d}t} = \dot{J}_{\rm wind}. \quad (14)$$

Here,

$$j_{\rm ISCO} = (GM_\bullet r_{\rm ISCO})^{1/2} \times \frac{r_{\rm ISCO}^2 - a_\bullet r_g (r_{\rm ISCO} r_g/2)^{1/2} + a_\bullet^2 r_g^2/4}{r_{\rm ISCO}[r_{\rm ISCO}^2 - 3r_{\rm ISCO} r_g/2 + a_\bullet r_g (r_{\rm ISCO} r_g/2)^{1/2}]^{1/2}} \quad (15)$$

is the specific angular momentum of a fluid element at the ISCO of the BH with mass $M_\bullet$, spin $a_\bullet = cJ_\bullet/GM_\bullet^2$, and gravitational radius $r_g = 2GM_\bullet/c^2$ (Bardeen et al. 1972). Mass is accreted onto the BH at the rate

$$\dot{m}_{\rm acc} = f_{\rm acc}\frac{M_{\rm disk}}{t_{\rm visc}}, \quad (16)$$

where

$$t_{\rm visc} = \alpha^{-1}\Omega_{\rm K,disk}^{-1} h_{\rm z,disk}^{-2} \quad (17)$$

is the viscous timescale of the disk, with α being the standard dimensionless disk viscosity (Shakura & Sunyaev 1973),

$$\Omega_{\rm K,disk}(t) = (GM_\bullet/r_{\rm disk}^3)^{1/2} \quad (18)$$

is the Keplerian angular velocity of the disk, and $h_{\rm z,disk}$ is its scale height (we take $h_{\rm z,disk} \approx 0.5$ as a fiducial value). The disk radius $r_{\rm disk}(t)$ is defined by the current disk mass and angular momentum,

$$j_{\rm disk} \equiv (GM_\bullet r_{\rm disk})^{1/2} = \frac{J_{\rm disk}}{M_{\rm disk}}. \quad (19)$$

The disk accretion flow gives rise to powerful outflows with the mass-loss rate

$$\dot{m}_{\rm wind} = (1 - f_{\rm acc})\frac{M_{\rm disk}}{t_{\rm visc}} \quad (20)$$

and the associated angular momentum loss rate

$$\dot{J}_{\rm wind} = \dot{m}_{\rm wind} j_{\rm disk}. \quad (21)$$

We do not include the interaction of such outflows with the infalling stellar envelope, which is beyond the scope of the present model. Investigating these effects would require detailed hydrodynamical simulations. However, we argue in Appendix C that these disk winds are powerful enough to

overcome the ram pressure of the infalling material in the polar directions, and are thus able to break out of the collapsing envelope, even without the help of a GRB jet.

Neutrinos effectively cool the disk above the critical "ignition" accretion rate for weak interactions (Chen & Beloborodov 2007; Metzger et al. 2008; Siegel et al. 2019; De & Siegel 2020), which is approximately given by (see Appendix A.1)

$$\dot{M}_{\rm ign} \approx 2 \times 10^{-3} M_\odot \,{\rm s}^{-1} \left(\frac{\alpha}{0.02}\right)^{5/3} \left(\frac{M_\bullet}{3M_\odot}\right)^{4/3}. \quad (22)$$

Motivated by the findings of GRMHD simulations of neutrino-cooled accretion flows (Siegel & Metzger 2018; Fernández et al. 2019; Siegel et al. 2019; De & Siegel 2020), we assume that for high accretion rates $>\dot{M}_{\rm ign}$, a fraction $1-f_{\rm acc} \approx 0.3$ of the disk mass is unbound in outflows. This fraction is assumed to increase to ≈ 0.6 below $\dot{M}_{\rm ign}$, under the assumption that inefficient cooling will result in excess heating and outflow production (e.g., Blandford & Begelman 1999; De & Siegel 2020). Similarly, we assume that enhanced outflow production also occurs at very high accretion rates for which neutrinos become effectively trapped in the optically thick accretion disk and are advected into the BH before radiating. This threshold "trapping" accretion rate is given by (see Appendix A.3)

$$\dot{M}_{\nu,{\rm trap}} \approx 1 M_\odot \,{\rm s}^{-1} \left(\frac{\alpha}{0.02}\right)^{1/3} \left(\frac{M_\bullet}{3M_\odot}\right)^{4/3}. \quad (23)$$

Insofar as $\dot{M}_{\nu,{\rm trap}}$ scales with the (growing) BH mass in the same way as $\dot{M}_{\rm ign}$, we find that this trapped regime is of little practical importance in our models. In summary, the accretion efficiency is given by

$$f_{\rm acc} = \begin{cases} 0.4, & \dot{M}_{\nu,{\rm trap}} \leqslant \dfrac{M_{\rm disk}}{t_{\rm visc}} \\ 0.7, & \dot{M}_{\rm ign} < \dfrac{M_{\rm disk}}{t_{\rm visc}} < \dot{M}_{\nu,{\rm trap}}. \\ 0.4, & \dfrac{M_{\rm disk}}{t_{\rm visc}} \leqslant \dot{M}_{\rm ign} \end{cases} \quad (24)$$

Equations (9)–(14) allow a calculation of the total ejecta mass $M_{\rm ejecta}$ obtained from a particular collapsar model. We evolve this set of coupled differential equations numerically, until all the stellar progenitor material has collapsed and has either been accreted onto the BH or been ejected into outflows. Note that these equations explicitly conserve mass and angular momentum. The time stepping is equidistant in $\log t$ and chosen to be sufficiently high such that (i) the accuracy of the total fallback mass is dominated by the radial resolution of the provided stellar model (see Appendix D), and (ii) the conservation of the total mass and angular momentum in Equations (9)–(14) is achieved at better than 10^{-14} relative accuracy for all model runs.

Once a disk forms around the BH and its accretion rate $\dot{m}_{\rm acc}$ exceeds $10^{-4}\,M_\odot\,{\rm s}^{-1}$, we assume that a relativistic jet emerges, which is powerful enough to drill through the remaining outer layers in the polar region. This threshold is motivated by the typical GRB luminosities $L_\gamma \sim 2 \times 10^{50}\,{\rm erg\,s^{-1}}$ (Goldstein et al. 2016), which, if accretion-powered, require an accretion rate of at least $\dot{M} \sim L_\gamma/c^2 \sim 1.1 \times 10^{-4}\,M_\odot\,{\rm s}^{-1}$. If this threshold is surpassed, we ignore any remaining material in the polar regions $\theta < \theta_{\rm jet}$ and $\theta > 180^\circ - \theta_{\rm jet}$ for the subsequent fallback process. This material has little effect on the total quantity of the material accreted through the disk, as it predominantly falls into the BH directly, due to the low angular momentum in these regions. However, it has a slight indirect effect on nucleosynthesis, by modifying the BH mass (see below). As a fiducial value, we take $\theta_{\rm jet} = 30^\circ$. We further justify the existence of such a successful jet a posteriori by the fact that our models reach the regime $\dot{M} > 10^{-4}\,M_\odot\,{\rm s}^{-1}$, which is favorable for powering typical observed long GRBs, including the time necessary for the jet to drill through the stellar envelope (see Section 2.3).

The fallback process may in some cases give rise to massive gravitationally unstable accretion disks. At this limit, the disk mass becomes comparable to the BH mass, and our assumption of a Kerr metric would no longer be justified. We estimate this instability region by monitoring the ratio of self-gravity to external gravitational acceleration by the BH potential (Paczynski 1978; Gammie 2001),

$$Q^{-1} \equiv \frac{2\pi\Sigma r_{\rm disk}^2}{M_\bullet h_{z,{\rm disk}}} \simeq \frac{2}{h_{z,{\rm disk}}} \frac{M_{\rm disk}}{M_\bullet} > 1, \quad (25)$$

where Σ is the disk's surface density. If $Q < 1$, we remove the excess disk mass by enhancing the accretion and wind production so as to restore $Q = 1$. This is motivated by the fact that gravitationally unstable disks tend to self-regulate by increased angular momentum transport via gravitationally driven turbulence, thereby increasing the accretion rate and reducing the disk mass until $Q > 1$ (e.g., Gammie 2001).

The composition of the disk wind ejecta at a given time depends most sensitively on the instantaneous accretion rate (Siegel et al. 2019). Following Siegel et al. (2019), Miller et al. (2020), and Li & Siegel (2021), we define the following accretion regimes:

$$\frac{M_{\rm disk}}{t_{\rm visc}} = \begin{cases} > \dot{M}_{\nu,{\rm r-p}} & \text{limited } r-\text{process}, \\ & (69 \leqslant A \leqslant 136) \\ \in [2\dot{M}_{\rm ign}, \dot{M}_{\nu,{\rm r-p}}] & \text{main } r-\text{process}, \\ & (69 \leqslant A) \\ \in [\dot{M}_{\rm ign}, 2\dot{M}_{\rm ign}] & \text{limited } r-\text{process}, \\ & (69 \leqslant A \leqslant 136) \\ < \dot{M}_{\rm ign} & \text{no } r-\text{process}, \\ & {}^{56}\text{Ni production} \end{cases} \quad (26)$$

Here, A denotes the mass number of the nuclei created, while $\dot{M}_{\nu,{\rm r-p}}$ represents the threshold between the production of lanthanides ($136 \lesssim A \lesssim 176$) and the first-to-second peak r-process elements ($69 < A \leqslant 136$) only, accounting for the fact that increased neutrino irradiation at high accretion rates tends to raise the electron fraction above ≈ 0.25, which is required for lanthanide production (e.g., Lippuner & Roberts 2015). We assume that this threshold scales with the accretion rate above which the inner disk becomes optically thick to neutrinos, which we estimate as (see Appendix A.3)

$$\dot{M}_{\nu,{\rm r-p}} \approx 0.1 M_\odot \,{\rm s}^{-1} \left(\frac{\alpha}{0.02}\right) \left(\frac{M_\bullet}{3M_\odot}\right)^{4/3}. \quad (27)$$

This expression has been normalized using the numerical results from Siegel et al. (2019) and Miller et al. (2020) for $M_\bullet \approx 3M_\odot$. Additionally, including the effects of neutrino fast flavor conversions may increase $\dot{M}_{\nu,\mathrm{r-p}}$ significantly (Li & Siegel 2021), possibly up to $\approx 1M_\odot\ \mathrm{s}^{-1}$ or higher for such light BHs. We therefore treat the normalization as a free parameter, and explore different scenarios in which the value is scaled up by a factor of 10.

Below the ignition rate $\dot{M}_{\mathrm{ign}}$, r-process production ceases abruptly, and nucleosynthesis in the outflows with roughly equal numbers of neutrons and protons ($Y_e \simeq 0.5$) only proceeds up to iron-peak elements (Siegel et al. 2019). A large fraction of the outflowing material in this epoch remains as ^{4}He, however, instead of forming heavier isotopes. This is due to the slow rate of the triple-α reaction needed to create seed nuclei when $Y_e \approx 0.5$, relative to the much faster neutron-catalyzed reaction $^4\mathrm{He}(\alpha n, \gamma)^9\mathrm{Be}(\alpha, n)^{12}\mathrm{C}$ that operates when $Y_e \ll 0.5$ (Woosley & Hoffman 1992). Here, we employ a simple model to estimate the yield of ^{56}Ni in such $Y_e \simeq 0.5$ disk outflows, similar to that of Siegel et al. (2019; see Appendix B).

A requisite for the synthesis of ^{56}Ni in disk outflows is that the nuclei from stellar fallback material are dissociated into individual nucleons once they enter the inner part of the accretion disk. At late times in the accretion process, the disk densities and temperatures may not be high enough to ensure full dissociation. We estimate the transition time t_{diss} to this state, by evaluating the conditions under which only 50% of the α particles are dissociated in the disk (see Appendix B). For $t > t_{\mathrm{diss}}$, we ignore any potential further nucleosynthesis in disk outflows.

For our light-curve models (Section 3), we further decompose the total (integrated) ejecta content of a given collapsar model into mass fractions of several constituents of interest. Assuming the full mixing of all ejecta content (see Section 3.1), we calculate the mass fraction X_{La} of the lanthanides ($136 \lesssim A \lesssim 176$), based on the amount of the main r-process material, assuming the solar r-process abundance pattern (Arnould et al. 2007) motivated by the results of Siegel et al. (2019). The mass fraction X_{lrp} for light r-process elements is based on a combined mass fraction of limited r-process material only plus the fraction of main r-process ejecta with $A < 136$ when applying the solar r-process abundance pattern. Finally, we also compute the mass fraction X_{Ni} of ^{56}Ni.

2.3. Collapsar Model Results

We start Section 2.3.1 by walking through the evolution of the collapse and mass ejection process for a representative model, corresponding to a star above the nominal PI mass gap. Appendix E presents the results of our model when applied to "ordinary" low-mass collapsars (with BH masses below the PI mass gap), demonstrating that for the fiducial range of parameters considered in this work, we obtain properties in agreement with observed GRBs and previously predicted r-process ejecta. Using the same parameters (now "calibrated" to reproduce the properties of ordinary collapsars), we present in Section 2.3.2 a parameter exploration of the ejecta masses and nuclear compositions for massive collapsars above the PI mass gap.

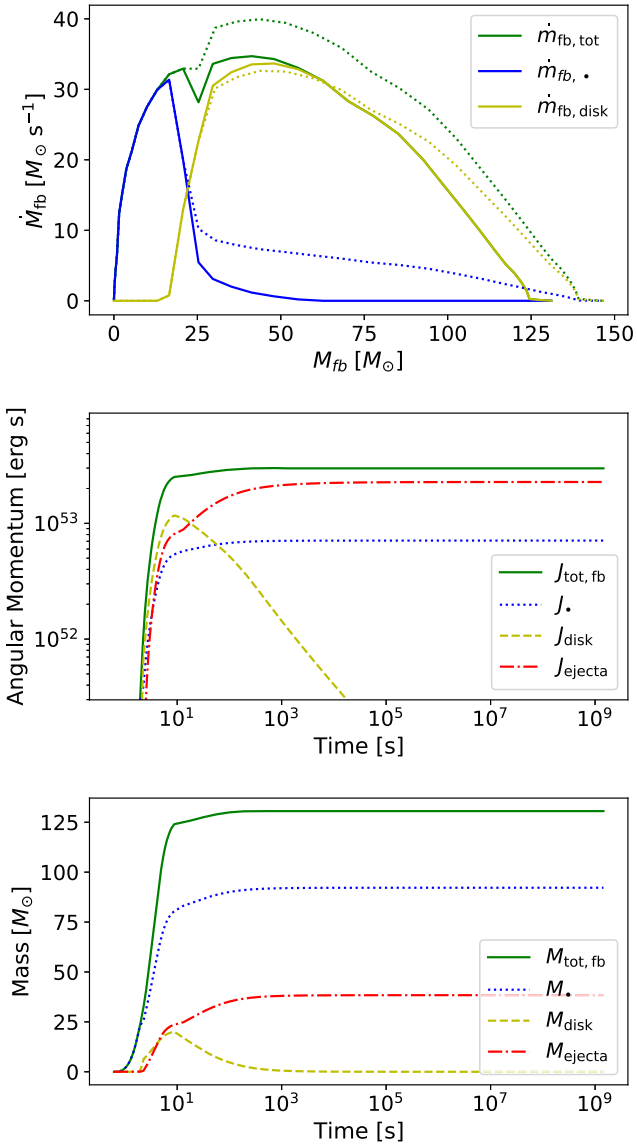

Figure 2. Collapse evolution for a representative stellar model, `250.25`, with the typical rotation parameters $p = 4.5$, $f_{\mathrm{K}} = 0.3$, and $r_{\mathrm{b}} = 1.5 \times 10^9$ cm. Top: fallback rates $\dot{M}_{\mathrm{fb}}$ onto the BH (blue; direct), onto an accretion disk (yellow), and in total (green), as a function of the total cumulative collapsed mass M_{fb}. The dotted lines indicate the corresponding evolution when ignoring the effect of a jet. Center and bottom: evolution of the angular momenta (center) and masses (bottom), as determined by Equations (9)–(14).

2.3.1. Basic Model Evolution

Figure 2 illustrates the collapse evolution of model `250.25`, with representative rotation parameters of $p = 4.5$, $f_{\mathrm{K}} = 0.3$, and $r_{\mathrm{b}} = 1.5 \times 10^9$ cm. At the formation of the seed BH, the BH grows rapidly in mass and spin, due to low–angular momentum material at small radii falling directly into the seed BH, before circularizing. Only after a few seconds, and the accretion of $\approx 10\,M_\odot$ of the inner layers, the material starts to circularize outside the BH horizon, to form an accretion disk (see Figure 2, top and bottom panels), which initiates accretion onto the BH through a disk, in addition to direct infall.

In this model, direct fallback onto the BH subsides after the accretion of about $20\,M_\odot$ (see Figure 2, top panel), when a significant fraction of the low–angular momentum material residing in the polar region of the progenitor model has fallen

into the BH. Further BH growth then proceeds almost entirely through disk accretion. This initial episode of direct fallback partially clears up the polar regions, allowing a relativistic jet to propagate through the outer stellar layers and eventually break out of the star, generating a long GRB. At around the same time, a significant fallback rate onto the disk sets in (see Figure 2, top panel), establishing a heavy $\sim 15\,M_\odot$ accretion disk on a timescale of a few seconds (see Figure 2, bottom panel). The disk accretion rate onto the BH, $\dot{m}_{\rm acc}$, quickly exceeds $\dot{M}_{\rm ign}$, and we assume that a relativistic jet forms. This removes the remaining low–angular momentum material in the polar regions, and thus results in the suppression of direct fallback onto the BH, which becomes negligible compared to the disk fallback (see Figure 2, top panel).

The top panel of Figure 2 also shows that ignoring the effect of such a jet would lead to subdominant extended direct fallback of the residual low–angular momentum material in polar regions onto the BH. While this does not have a direct impact on disk accretion, it has minor indirect consequences on nucleosynthesis in the disk winds, due to its effect on the BH mass (see Equation (26)). For somewhat larger values of $r_{\rm b}$, the situation changes, and direct fallback onto the BH may extend to late times, even in the presence of a jet, due to the overall lower angular momentum budget of the progenitor star outside the polar cone with opening angle $\theta_{\rm jet}$. For more extreme scenarios, fallback onto the disk may become close to nonexistent.

In this model, as soon as the disk forms, most of the angular momentum resides in the disk, rather than in the BH (see Figure 2, center panel). The majority of this is being blown off in the ejecta, while a subdominant amount is transferred to the BH, as disk matter gradually accretes through the ISCO onto the BH. For significantly larger values of r_b, this trend reverses, and most angular momentum is transferred to the BH, rather than the ejecta, as less material accretes through a disk.

The top panel of Figure 3 presents the history of the ejecta production in the model discussed above. The instantaneous accretion state $M_{\rm disk}/t_{\rm visc}$ of the disk as a function of the cumulative ejected wind mass is shown, together with the nucleosynthesis regimes defined in Equation (26). This evolution shows a "sweep" through most nucleosynthesis regimes, typical of the models considered here. The nucleosynthesis regimes change over the course of the evolution as a result of the BH mass growth, and in some cases they can be more dramatic than the illustration here. Outflows are first created in the regime of the main r-process with lanthanide production, during which the bulk of the wind ejecta are produced. The remaining $\approx 10\,M_\odot$ of ejecta originate in a regime that mostly ejects α-particles and $\sim 0.1\,M_\odot$ of ^{56}Ni. The bottom panel of Figure 3 illustrates ^{56}Ni production in this regime. The mass fraction of ^{56}Ni produced in disk outflows according to Equation (B2) is shown, as well as the mass fraction of α-particles in the accretion disk according to Equation (B6). The vertical dashed line indicates the dissociation time $t_{\rm diss}$ after which $< 50\%$ of the α-particles are dissociated into individual nucleons in the accretion disk (Section 2.2; Appendix B). As a conservative estimate, for $t > t_{\rm diss}$, we ignore any further production of ^{56}Ni according to Equation (B2), as the required free nucleons become unavailable. However, in most cases this represents only a slight correction, as a dominant amount of ^{56}Ni is typically produced before $t = t_{\rm diss}$.

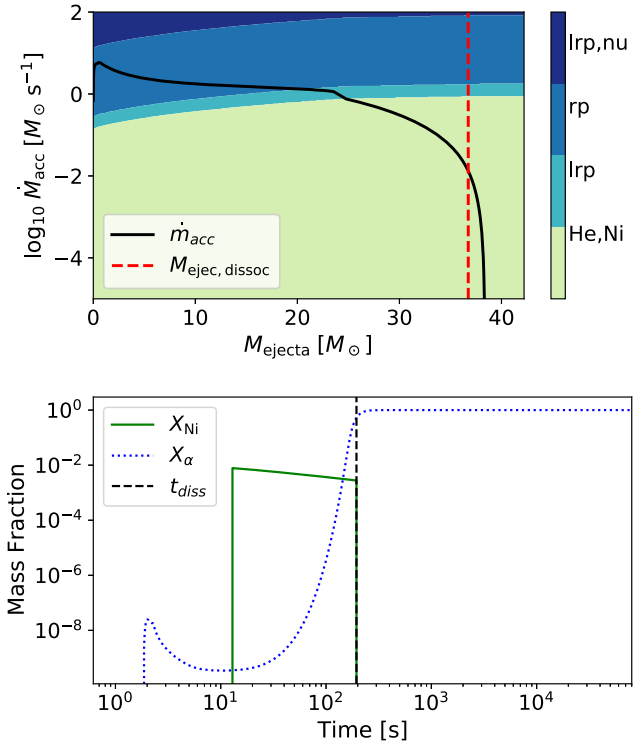

Figure 3. Top: the accretion rate at which the ejecta are being produced as a function of the cumulative ejecta mass for model `250.25`, with $p = 4.5$, $f_{\rm kep} = 0.3$, and $r_{\rm b} = 1.5 \times 10^9$ cm. The nucleosynthesis regimes according to Equation (26) are color-coded (from top to bottom, in the same order as in Equation (26)). The red dashed line indicates the cumulative mass ejected until $t = t_{\rm diss}$ (see below). Bottom: the corresponding mass fractions of ^{56}Ni synthesized in disk outflows and ^{4}He in the accretion disk. The production of ^{56}Ni sets in at around ≈ 10 s, when the accretion rate enters the light green regime in the top panel (the fourth accretion regime in Equation (26)). The vertical dashed line indicates the time $t_{\rm diss}$ at which only 50% of the α-particles are dissociated in the disk. For $t > t_{\rm diss}$, we ignore further ^{56}Ni production in the outflows.

2.3.2. Parameter Study of Massive Collapsars

Before systematically applying our model across the parameter space of massive collapsars, we first apply it to "ordinary" collapsars of stars well below the PI mass gap, with the results being described in Appendix E. We use the progenitor models of Heger et al. (2000), as representative of typical stellar progenitors of canonical long GRBs (MacFadyen & Woosley 1999). Our results for the nucleosynthesis yields of the disk outflows as a function of the parameters $\{f_{\rm K},\ r_{\rm b}\}$, which enter the progenitor angular momentum profile (Figure 18), broadly agree with those previously presented in Siegel et al. (2019), although some quantitative differences arise, due to our more detailed treatment of the different regimes of BH accretion (see Appendix E for a discussion). Our low-mass collapsar models also exhibit BH accretion timescales and energetics of putative jet activity that are in agreement with long-GRB observations. We can therefore claim the rough "calibration" of our model across the adopted parameter space of progenitor angular momentum properties, allowing for more confidence when extrapolating to the regime of more massive collapsars, as described below.

Figures 4 and 20 summarize our results for the ejecta and GRB properties for model `250.25`, as a representative example of a stellar model above the PI mass gap, in the parameter space $\{f_{\rm K},\ r_{\rm b}\}$. The top panel of Figure 4 shows that, even for the

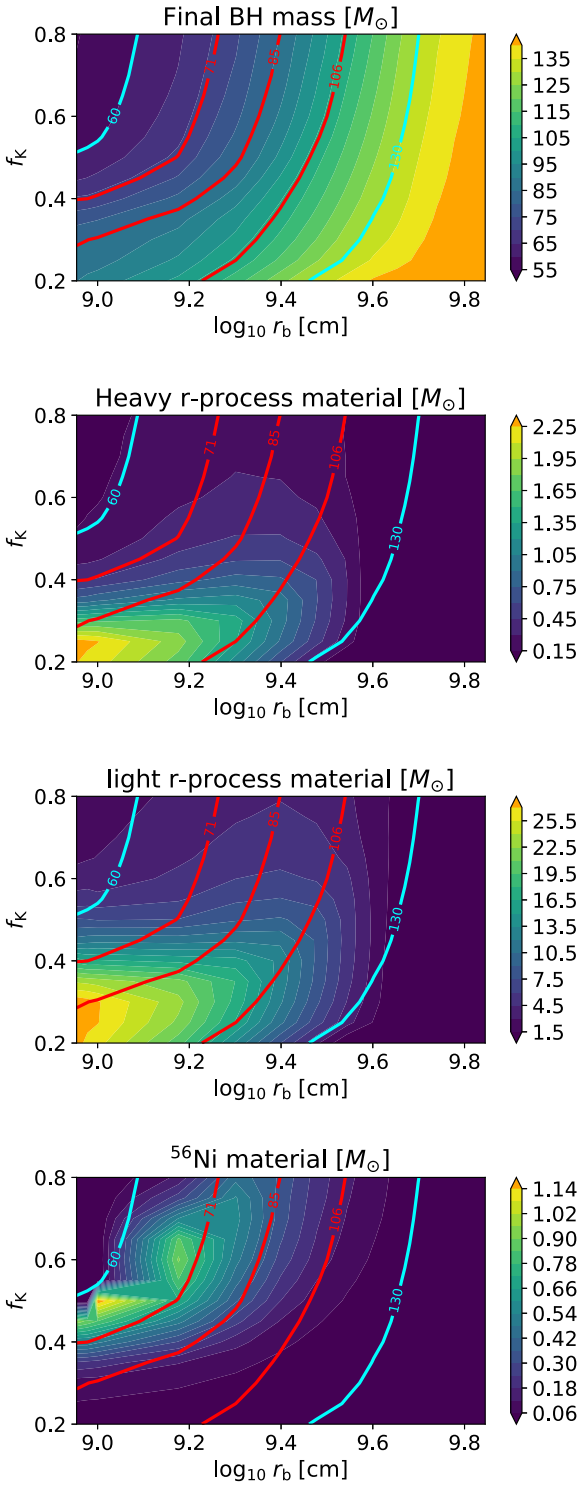

Figure 4. BH masses and disk wind ejecta properties across the parameter space of progenitor rotational profiles (envelope Keplerian fraction f_K and break radius r_b, $p = 4.5$; see Figure 1, bottom panel) for model `250.25`. The final BH mass (top), the total ejected mass in heavy ($A > 136$) *r*-process elements, including lanthanides (center top), the light ($A < 136$) *r*-process material (center bottom), and ^{56}Ni (bottom) are shown. The red contours indicate the inferred primary mass of GW190521, together with its 90% confidence limits ($85^{+21}_{-14}\,M_\odot$; Abbott et al. 2020). The cyan contours delineate the final BH masses of 60 $M_\odot$ and 130 $M_\odot$, which approximately correspond to the lower and upper end of the PI mass gap.

progenitor mass $M_\star = 150\,M_\odot$ at the onset of collapse (that is, well above the PI mass gap), the final BH remnant can populate the entire mass gap between $\sim 55\,M_\odot$ and $130\,M_\odot$ (for typical parameter values), depending on the rotation profile at the onset of collapse. The labeled contours indicate the inferred primary masses of GW190521, together with their 90% confidence limits. We focus on this region of the parameter space in the following, insofar as the superKNe generated from such events probe BHs that are formed in the PI mass gap.

As in case of the low-mass collapsars (Appendix E), our results are not sensitive to the precise value of the power-law coefficient p, which we thus ignore in what follows. We find ubiquitous *r*-process production throughout the parameter space, ranging between ~ 0.1 and $2.3\,M_\odot$ of heavy ($A > 136$) *r*-process material, including lanthanides, and ~ 1–$29\,M_\odot$ of light ($A < 136$) *r*-process elements. Additionally, between ~ 0.05 and $1\,M_\odot$ of ^{56}Ni is synthesized in the ejecta.

Interestingly, the region of the highest *r*-process production is well aligned with the intermediate final BH masses in a range similar to the GW190521 confidence region (Section 5.3). For large r_b, the outer stellar layers possess too little angular momentum to form massive accretion disks that give rise to copious *r*-process ejecta, as most material falls directly into the BH. On the other hand, for small values of r_b and high values of f_K, massive disks form; however, high angular momentum leads to large disk radii r_{disk} and associated viscous timescales, such that the accretion rate drops below the required threshold for *r*-process production for most of the accretion process. This occurs despite the presence of spiral modes in this regime, which tend to increase the accretion rate (Section 2.2). Most *r*-process material (both light and heavy) is synthesized for small values of both r_b and f_K, which represents the optimal compromise between high angular momentum and the sufficient compactness of the accretion disk. We discuss the possible contribution of massive collapsars to the long-GRB population in Section 4.3.

Results for the mass fractions of lanthanides, the light and heavy r-process elements, as well as ^{56}Ni are depicted in Figure 5. For concreteness, we select several models along isomass contours for the final BH mass within the GW190521 confidence region, and report the corresponding ejecta parameters in Table 1.

3. SuperKN Emission

As the disk outflows expand away from the BH, the ejecta shell that they form eventually gives rise to optical/IR emission powered by radioactive decay (the superKN).

3.1. Analytic Estimates

We begin with analytic estimates of the superKN properties. The total ejecta mass M_{ej} is comprised of up to three main components: (1) radioactive *r*-process nuclei, with mass fraction X_{rp}; (2) radioactive ^{56}Ni, X_{Ni}; and (3) nonradioactive ^{4}He, $X_{He} = 1 - X_{rp} - X_{Ni}$ (also a placeholder for other nonradioactive elements). The typical values for our fiducial models (Section 2.3) are $M_{ej} \sim 10$–$60 M_\odot$, $X_{rp} \sim 0.1$–0.5, and $X_{Ni} \sim 10^{-3}$–10^{-2} ($M_{Ni} \sim 10^{-2}$–$0.5 M_\odot$). As described in the previous section, the total *r*-process mass fraction can be further subdivided into light *r*-process nuclei X_{lrb} and lanthanides X_{La}. For simplicity, we assume throughout this section that the ejecta are mixed homogeneously into a single approximately spherical shell. Physically, such mixing could result from hydrodynamic instabilities that develop between

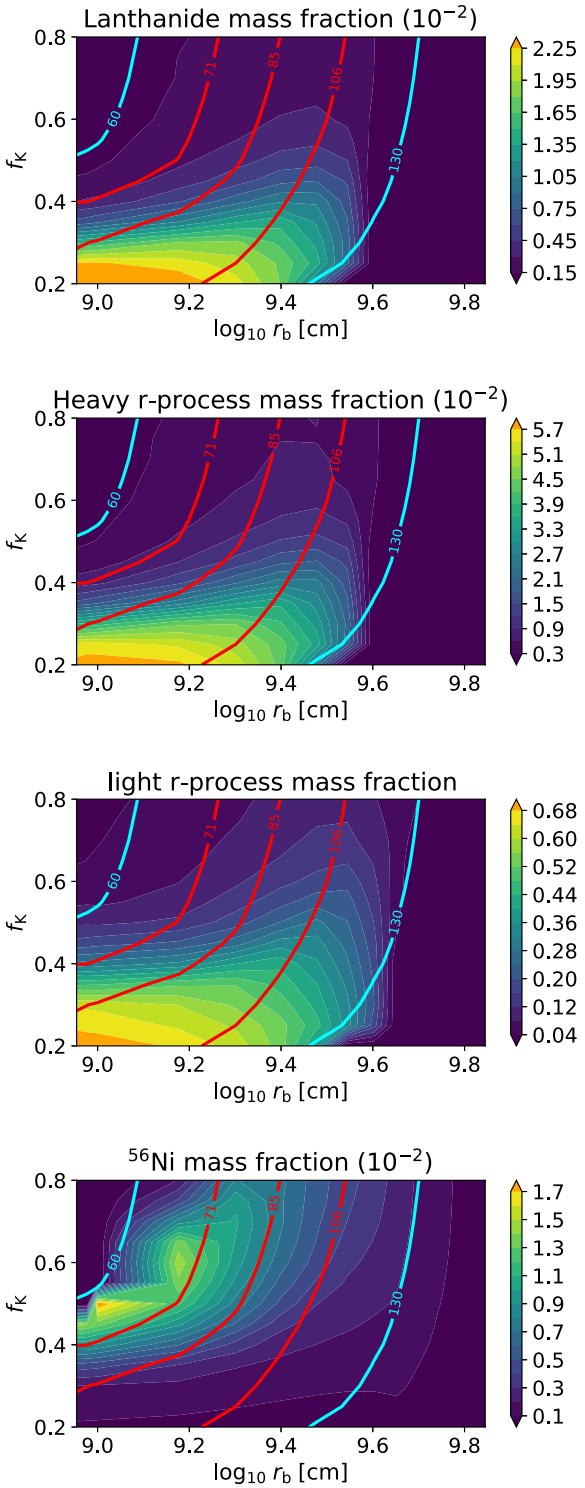

Figure 5. Scan of the parameter space for model `250.25`, setting $p = 4.5$. We show the mass fractions of lanthanides (top), the heavy r-process elements (A $>$ 136; center top), the light r-process elements ($A < 136$; center bottom), and ^{56}Ni (bottom) in the ejecta, assuming the full mixing of ejecta components. The red contours indicate the inferred primary mass of GW190521, together with its 90% confidence limits. The cyan contours delineate final BH masses of 60 $M_\odot$ and 130 $M_\odot$, which approximately correspond to the lower and upper end of the PI mass gap.

different components of the radial and temporally dependent disk winds and/or be due to its interaction with the GRB jet (e.g., Gottlieb et al. 2021). Furthermore, a high degree of mixing is expected to be more common among superKN ejecta, as compared to those "ordinary" low-mass collapsars that produce Type Ic SNe with broad lines (Ic-bl). This is because the very massive envelopes present in superKNe are unlikely exploded by a protomagnetar, and thus likely require interaction with disk outflows to become unbound (Appendix C). As a result, a high degree of mixing of disk outflows with envelope material is expected. In contrast, many low-mass collapsars may be exploded by a protomagnetar or the GRB jet even prior to the formation of significant disk outflows, and the subsequently ejected disk winds will then mix less efficiently with the envelope material, as compared to superKNe. A radial stratification of the lanthanide content in ordinary collapsars is thus conceivably more common, and such stratification is an important determinant of the emission from a low-mass r-process-enriched collapsar (Barnes & Metzger 2022). If, however, the ejecta in superKNe maintain a radial stratification, with a low lanthanide abundance and thus low opacity in the outermost layers, the early light curve could be significantly bluer than the estimates presented in this section.

The light curve will peak roughly when the expansion timescale equals the photon diffusion timescale (e.g., Arnett 1982):

$$t_{\rm pk} \approx \left(\frac{M_{\rm ej}\kappa}{4\pi v_{\rm ej} c}\right)^{1/2} \approx 108\ {\rm d}\left(\frac{M_{\rm ej}}{50 M_\odot}\right)^{1/2}\left(\frac{v_{\rm ej}}{0.1c}\right)^{-1/2}\left(\frac{\kappa}{1{\rm cm^2\ g^{-1}}}\right)^{1/2}, \quad (28)$$

where $v_{\rm ej}$ is the average ejecta velocity. The effective gray opacity κ varies in kilonovae from $\lesssim$1 cm^2 g^{-1}, for ejecta dominated by light r-process species, to $\sim$10–30 cm^2 g^{-1}, for ejecta containing a sizable quantity of lanthanide atoms and ions (e.g., Kasen et al. 2013; Tanaka et al. 2020). However, κ will be smaller than these estimates in the superKN case, due to the large mass fraction of light elements, $X_{\rm He} \sim 0.5$–0.9, which contribute negligibly to the opacity. For our analytical estimates below, we linearly interpolate κ between 0.03 cm^2 g^{-1} (at $X_{\rm La} = 10^{-4}$) and 3 cm^2 g^{-1} (at $X_{\rm La} \geqslant 0.2$), which we find results in reasonable agreement with the detailed radiation transport calculations present in Section 3.2.

The peak luminosity and effective temperature can also be estimated using analytic formulae (e.g., Metzger 2019):

$$L_{\rm pk} \approx 4 \times 10^{41}{\rm erg\ s^{-1}}\left(\frac{X_{\rm rp}}{0.2}\right) \times \left(\frac{M_{\rm ej}}{50 M_\odot}\right)^{0.35}\left(\frac{v_{\rm ej}}{0.1c}\right)^{0.65}\left(\frac{\kappa}{\rm cm^2\ g^{-1}}\right)^{-0.65}, \quad (29)$$

$$T_{\rm eff,pk} \approx 900\ {\rm K}\left(\frac{X_{\rm rp}}{0.2}\right)^{0.25} \times \left(\frac{M_{\rm ej}}{50 M_\odot}\right)^{-0.16}\left(\frac{v_{\rm ej}}{0.1c}\right)^{-0.09}\left(\frac{\kappa}{\rm cm^2\ g^{-1}}\right)^{-0.41}, \quad (30)$$

where we have used the radioactive heating rate of r-process nuclei from Metzger et al. (2010), with an assumed thermalization efficiency of 50%. Near the peak light $t \sim t_{\rm pk} \sim 100$ days, the specific radioactive heating rate of ^{56}Ni is $\sim$10–30 times higher than that of r-process elements (e.g.,

Table 1
Ejecta Parameters for Select Mass Gap Collapsar Models with $p = 4.5$ along Contours of Constant Final BH Mass (see Figures 4 and 5)

Model	$M_\bullet$ ($M_\odot$)	$M_{\rm ej}$ ($M_\odot$)	$r_{\rm b}$ (10^9 cm)	$f_{\rm K}$	$X_{\rm La}$	$X_{\rm lrp}$	$X_{\rm Ni}$	$X_{\rm Ni}/X_{\rm rp}$
250.25	106	27.24	1.94	0.25	0.020	0.59	0.0011	0.0018
	106	29.67	2.35	0.35	0.014	0.47	0.0020	0.0041
	106	30.51	2.67	0.45	0.008	0.36	0.0028	0.0075
	106	31.53	3.04	0.60	0.004	0.21	0.0039	0.0179
	85	45.57	1.20	0.35	0.012	0.47	0.0040	0.0079
	85	46.25	1.69	0.45	0.007	0.32	0.0059	0.0175
	85	47.20	1.96	0.55	0.005	0.22	0.0070	0.0303
	85	47.48	2.06	0.60	0.004	0.19	0.0072	0.0359
	71	58.06	1.19	0.50	0.004	0.19	0.0120	0.0601
	71	58.22	1.37	0.55	0.003	0.16	0.0094	0.0562
	71	58.00	1.50	0.60	0.003	0.13	0.0058	0.0417
	71	59.78	1.53	0.65	0.002	0.11	0.0121	0.1035
200.25	106	11.41	2.14	0.25	0.011	0.42	0.0013	0.0029
	106	13.87	2.59	0.35	0.008	0.34	0.0019	0.0054
	85	28.77	1.32	0.35	0.016	0.53	0.0026	0.0046
	85	29.74	1.59	0.45	0.010	0.39	0.0040	0.0096
	71	40.93	1.07	0.50	0.007	0.29	0.0079	0.0254
	71	40.64	1.21	0.55	0.006	0.25	0.0083	0.0308

Siegel et al. 2019). Given the values $X_{\rm Ni}/X_{\rm rp} \sim 0.01$–$0.05$ for most of our disk outflow models, $L_{\rm pk}$ is moderately underestimated by Equation (29), which neglects ^{56}Ni heating.

Figure 6 shows the predicted peak timescale, luminosity, and effective temperature of the superKN emission in the parameter space $\{f_{\rm K}, r_{\rm b}\}$ for the fiducial model `250.25`. For the same parameters that generate remnant BHs with masses in the PI gap, we predict peak luminosities $L_{\rm pk} \sim 10^{42}$ erg s^{-1} and characteristic durations of months. Though similar to other types of SNe in duration, superKNe are characterized by significantly cooler emission ($T_{\rm eff} \approx 1000$ K), as confirmed by the radiative transfer calculations presented in the next section.

3.2. SuperKN Light Curves and Spectra

3.2.1. Model Selection and Parameters

To elaborate on the estimates of Section 3.1, we carried out detailed radiation transport simulations for five ejecta models, whose properties ($M_{\rm ej}$, $M_{\rm Ni}$, $M_{\rm lrp}$, and $M_{\rm La}$) span the space defined by the subset of simulations that produced BHs within the mass gap ($60 \lesssim M_\bullet/M_\odot \lesssim 130$), i.e., the models that fall between the two cyan contours of Figure 5 (see also Woosley 2017; Farmer et al. 2019, 2020; Renzo et al. 2020b; Costa et al. 2021; Mehta et al. 2022). As discussed in Section 3.1, we assume all constituents of the ejecta to be homogeneously mixed. The parameters of the mass gap models are largely confined to a plane in $M_{\rm ej}$–$M_{\rm Ni}$–$M_{\rm lrp}$–$M_{\rm La}$ space, making it straightforward to select a handful of characteristic parameters from the full set. We used the KMeans routine of `sklearn` (Pedregosa et al. 2011) to divide our models into four clusters, and we adopted the positions of the cluster centers as four representative superKNe models. However, a small fraction of the mass gap models occupy a distinct region of the parameter space, having large $M_{\rm ej}$, but few to no nucleosynthetic products heavier than He. Since these models were not captured by our clusters, we added a fifth model to explore the edge case of a high-mass nickel-free outflow. Our five models are listed in Table 2.

For the models in Table 2, we performed one-dimensional radiation transport calculations that were carried out with the Monte Carlo radiation transport code `Sedona` (Kasen et al. 2006; D. Kasen et al. 2022, in preparation). For each model, we adopted a density profile such that the mass external to the velocity coordinate v follows a power law:

$$M_{>v} \propto \left(\frac{v}{v_{\rm min}}\right)^{-\alpha}, \quad v \geqslant v_{\rm min}. \tag{31}$$

Above, the minimum ejecta velocity $v_{\rm min}$ is determined by the characteristic velocity $v_{\rm ej} = (2E_{\rm kin}/M_{\rm ej})^{1/2}$ (with $E_{\rm kin}$ being the ejecta kinetic energy) and the choice of power-law index α:

$$v_{\rm min} = \left(\frac{\alpha - 2}{\alpha}\right)^{1/2} v_{\rm ej}. \tag{32}$$

We take $\alpha = 2.5$ and $v_{\rm ej} = 0.1c$ for all models, consistent with predictions of accretion disk outflow velocities (e.g., Fernández et al. 2015; Siegel et al. 2019).

The opacity of the outflowing gas, and therefore the nature of the electromagnetic emission of the transients, is sensitive to the abundance pattern in the ejecta. Specifically, lanthanides and actinides, and, to a lesser extent, elements in the *d*-block of the periodic table, contribute a high opacity, while the opacities of *s*- and *p*-block elements are significantly lower (Kasen et al. 2013; Tanaka et al. 2020).

In this work, we predict the synthesis of helium, ^{56}Ni, and light and heavy *r*-process material, but do not carry out detailed nucleosynthesis calculations, e.g., by postprocessing fluid trajectories. The composition of each model is therefore solely a function of its $M_{\rm ej}$, $M_{\rm Ni}$, $M_{\rm lrp}$, and $X_{\rm La}$. We assume that heavy ($A > 136$) *r*-process material is 41% lanthanides and actinides by mass, equal to the solar value of $M_{\rm La}/M_{\rm A>136}$. The remainder is split between *d*-block and *s*-/*p*-block elements (54% and 5% by mass, respectively). For limited *r*-process material, $X_{\rm La} = 0$. We estimated that this comprises 95% (5%) *d*-block (*s*-/*p*-block) elements by mass.

The composition adopted for our radiation transport models is limited by both our imperfect knowledge of the details of nucleosynthesis and by incomplete atomic data of the sort necessary to calculate photon opacities in the ejecta. The lanthanide and actinide mass ($M_{\rm La}$) is divided among the

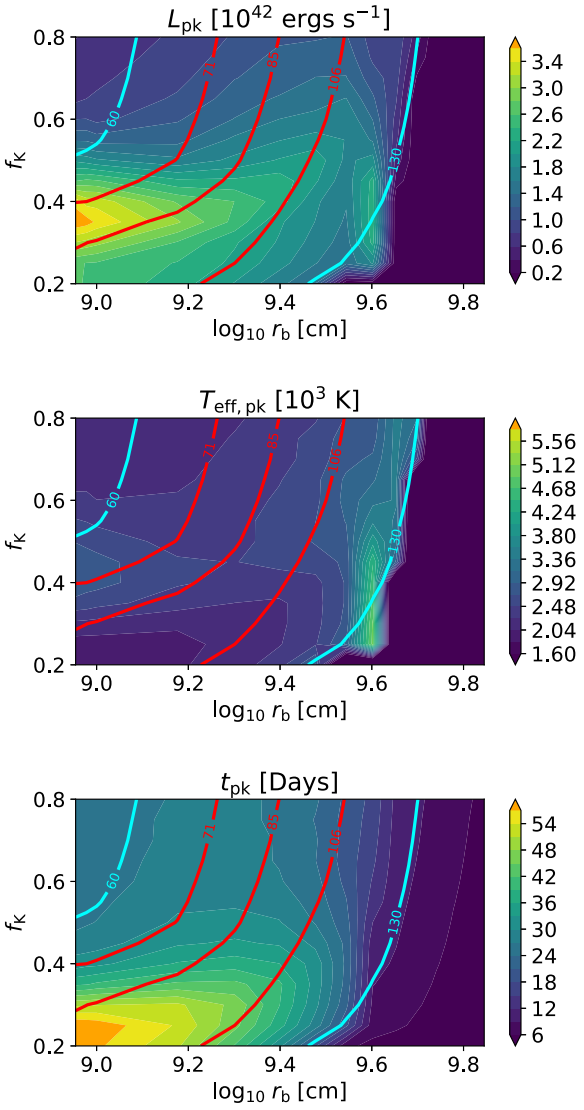

Figure 6. Analytic light-curve estimates across the parameter space for model `250.25`, setting $p = 4.5$. The peak luminosity (top), peak effective temperature (center), and peak timescale (bottom) are shown. The red contours indicate the inferred primary mass of GW190521, together with its 90% confidence limits. The cyan contours delineate final BH masses of 60 $M_\odot$ and 130 $M_\odot$, which approximately correspond to the lower and upper end of the PI mass gap.

lanthanide elements, following the solar pattern, with one adjustment: because the required atomic data is not available for atomic number $Z = 71$, we redistribute the solar mass fraction of $Z = 71$ to $Z = 70$.

Atomic data is also unavailable for most of the *d*-block elements produced by the *r*-process (whether heavy or light). We thus distribute the *d*-block mass evenly among the elements with $Z = 21$–28 (excluding $Z = 23$ due to the lack of data), artificially increasing the mass numbers to $A \sim 90$, to avoid overestimating the ion number density. All *r*-process *s*- and *p*-block material is modeled by the low-opacity filler Ca ($Z = 20$). ^{4}He and ^{56}Ni (as well as their daughter products ^{56}Co and ^{56}Fe) are straightforward to incorporate into the composition.

Our radiation transport simulations include radioactivity from both the ^{56}Ni decay chain and the *r*-process. We explicitly track energy loss by gamma rays from ^{56}Ni and ^{56}Co, and assume that the positrons from ^{56}Co decay thermalize immediately upon production. We model the *r*-process radioactivity by using the results of Lippuner & Roberts (2015) for an outflow with (Y_e, s_B, τ_{exp}) = (0.13, 32k_B, 0.84 ms), with s_B being the initial entropy per baryon and τ_{exp} the expansion timescale. To account for thermalization, we adjust the absolute radioactive heating rate, following the analytic prescription of Barnes et al. (2016).

Table 2
SuperKN Light-curve Models and Survey Detection Rates

Model	M_{ej} ($M_\odot$)	v_{ej} (c)	M_{Ni} ($M_\odot$)	M_{lrp} ($M_\odot$)	X_{La} (10^{-3})	R_{Rubin}[a] (yr^{-1})	$R^{(b)}_{Roman}$ (yr^{-1})
A	8.6	0.1	0.019	0.83	1.4	0.01	0.02
B	31.0	0.1	0.012	8.28	17.0	0.03	0.4
C	35.6	0.1	0.087	23.2	4.0	0.1	2
D	50.0	0.1	0.53	9.59	0.53	0.1	4
E	60.0	0.1	0.0	5.6	0.17	0.2	0.01

Note.
[a] [(b)] The detection rates per year from the Rubin Observatory and Roman, respectively, for an assumed $z = 0$ superKN rate of 10 Gpc^{-3} yr^{-1} (see Section 4.2 for details).

3.2.2. Radiation Transport Results

The bolometric light curves of models A through E are presented in Figure 7. For comparison, we also show the light curves of typical SNe of various subtypes: Type Ia SN 2011fe (Tsvetkov et al. 2013), Type Ic-bl SN 2002ap (Tomita et al. 2006), Type IIp SN 2013ab (Bose et al. 2015), and the electron-capture SN 2018dz (Hiramatsu et al. 2021).

The superKN light curves exhibit considerable diversity, which is not surprising, given the large ranges of ejecta and the radioactive masses that these systems may produce. As would be expected from simple Arnett-style arguments (Arnett 1982), higher masses are generally associated with longer light-curve durations. This can be seen in the progression from model A to model D.

However, as model E demonstrates, the shape of the light curve also depends on the presence of ^{56}Ni in the ejecta. While the mass of the *r*-process material burned in superKN outflows greatly exceeds that of ^{56}Ni, the energy generated by the ^{56}Ni decay chain, per unit mass, exceeds that of the *r*-process decay by orders of magnitude (e.g., Metzger et al. 2010; Siegel et al. 2019). When ^{56}Ni is present, it can be the main source of radiation energy for the transient. As a result of the long half-life of the ^{56}Ni daughter ^{56}Co ($\tau^{Co}_{1/2} \approx 77$ days), the energy generation rate for ^{56}Ni-producing systems declines slowly just around the time when the light curves reach their maxima. The effect is a more extended light curve (see Khatami & Kasen 2019 and Barnes et al. 2021 for more detailed discussions).

Model E, which produces no ^{56}Ni, has a relatively short ($\sim$month) duration, despite its high mass ($M_{ej} = 60 M_\odot$), owing to the steep decline of the *r*-process radioactivity that is its only source of energy. The qualitative difference between models that burn even small amounts of ^{56}Ni and models that burn none points to the importance of the careful treatment of nucleosynthesis in disk outflows.

As is apparent from Figure 7, the diversity of the superKN light curves allows them to mimic other types of SNe. While superKNe do not produce sufficient ^{56}Ni to approach the luminosity of SNe Ia, they can, at various epochs, mimic the bolometric light curves of SNe Ic-bl, SNe IIp, and electron-capture SNe. However, the high opacity of the *r*-process-

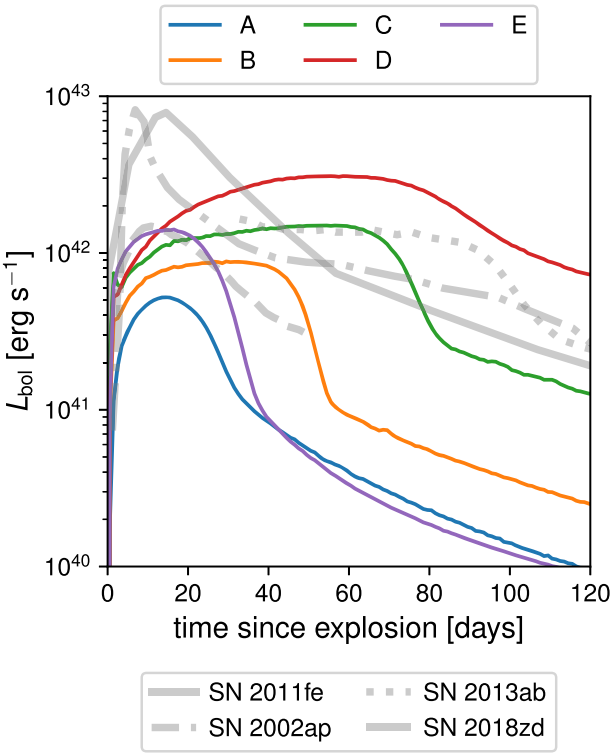

Figure 7. The bolometric light curves of the models in Table 2, compared to the prototypical SNe 2011fe (Type Ia), 2002ap (Type Ic-bl), 2013ab (Type II-p), and 2018zd (electron-capture). The superKN light curves are dimmer than the SNe Ia ones, but at some epochs they can approximate the light curves of SNe Type Ic-bl and Type IIp.

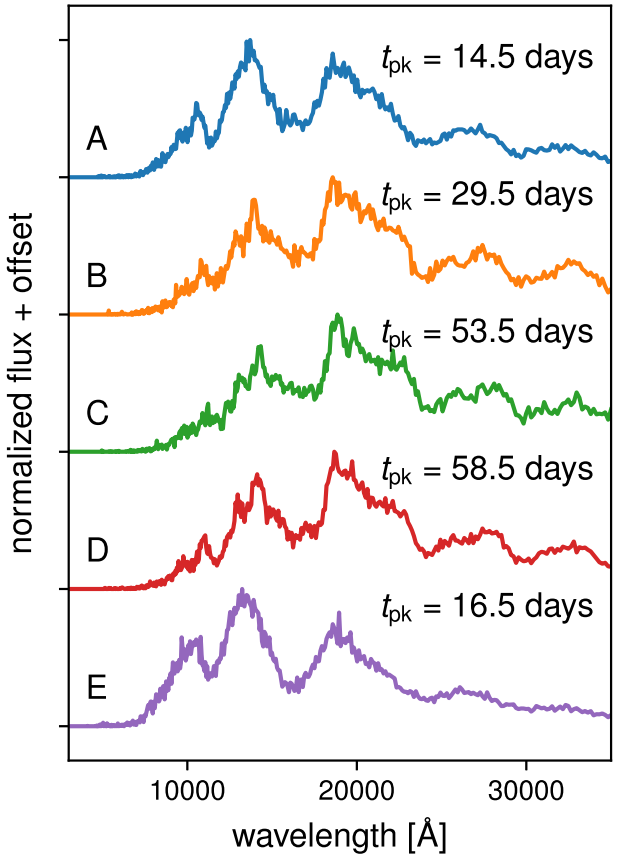

Figure 8. The flux per unit wavelength at bolometric peak for each of the five models defined in Table 2. All of the spectra have broad absorption features that are consistent with high-velocity outflows, and low-temperature pseudo-blackbody spectra, which are consistent with high-opacity compositions. These spectra distinguish superKNe from the other classes of SNe, which are much bluer, and from other dust-enshrouded explosions, in which broad absorption features are absent.

enriched ejecta pushes the superKN emission to redder wavelengths than are observed for the other classes of SNe. This is illustrated in Figure 8, which shows the normalized spectra for models A through E at bolometric peak.

Unlike other types of SNe, most of the superKN flux emerges at near- and even mid-IR wavelengths. This is likely due to a combination of lower radioactive heating per unit ejecta mass, as well as the high opacity from the r-process elements (particularly lanthanides and actinides) and the high $M_{\rm ej}$, which work in concert to increase the optical depth across the ejecta and push the photosphere out to the exterior, where temperatures are cooler.

A second distinguishing feature of superKNe is their broad absorption features. These are a product of our assumed ejecta velocities ($v_{\rm ej} = 0.1c$), which are higher than those inferred for all SNe, other than the hyperenergetic SNe Ic-bl. And while SNe Ic-bl produce spectra with similarly wide absorption features, these features, in the case of SNe Ic-bl, are found at much bluer (4000 Å $\lesssim\lambda\lesssim$ 8000 Å) wavelengths. Thus, despite their bolometric similarities, superKNe are spectroscopically unique among SNe.

The peak photospheric temperatures of superKNe $\sim$1000 K are also similar to those required for solid condensation, suggesting the possibility of dust formation in the ejecta (e.g., Takami et al. 2014; Gall et al. 2017). Insofar as the optical/near-IR opacity of $\sim$micron-sized dust is roughly comparable to that of lanthanide-enriched ejecta, dust formation would not qualitatively impact the appearance of the transient. However, this does imply potential degeneracy between the photometric signatures of superKNe and other dust-enshrouded explosions that are unrelated to r-process production, including stellar mergers (e.g., Kasliwal et al. 2017). This degeneracy with dusty transients can generally be broken by the predicted broad spectral features of superKNe ($v_{\rm ej} \sim 0.1c$).

4. Discovery Prospects

In this section, we explore the discovery prospects of superKNe in future optical/IR transient surveys and via late-time IR follow-up observations of energetic long GRBs. We then discuss how superKN emission could be enhanced by circumstellar interaction for collapsars embedded in active galactic nucleus (AGN) disks.

4.1. Volumetric Rates

We begin by estimating the volumetric rate of superKNe. One approach is to scale from the observed rates of ordinary collapsars. The local (redshift $z \simeq 0$) volumetric rate of classical long GRBs is $\approx$0.6–2 Gpc^{-3}yr^{-1} (Wanderman & Piran 2010); for an assumed gamma-ray beaming fraction $f_{\rm b} = 0.006$ (Goldstein et al. 2016), this corresponds to a total collapsar rate of $\approx$100–300 Gpc^{-3} yr^{-1}. Under the assumption that ordinary collapsars originate from stars of initial mass $M_{\rm ZAMS} \gtrsim 40M_\odot$, the more massive stars $M_{\rm ZAMS} \gtrsim 250M_\odot$ that generate helium core masses above the PI mass gap ($M_{\rm BH} \gtrsim 130M_\odot$) will be less common by at least a factor of $\sim (40/250)^{\alpha-1} \sim$ 0.1–0.3 for an

IMF $dN_\star/dM_\star \propto M_\star^{-\alpha}$, considering values for the power-law index between $\alpha = 2.35$, for a Salpeter IMF, and a shallower value $\alpha \approx 1.8$ (Schneider et al. 2018). This optimistically assumes that (i) stars that massive can exist (e.g., de Koter et al. 1997; Crowther et al. 2016), and that (ii) they can form helium cores such that $M_{\rm He} \simeq M_{\rm ZAMS}$, for instance, because of rotational mixing (e.g., Maeder & Meynet 2000; Marchant et al. 2016; de Mink & Mandel 2016) or the continuous accretion of gas (e.g., Cantiello et al. 2021; Dittmann et al. 2021; Jermyn et al. 2021). Various processes act to remove mass from a massive star during its evolution, and it is generally the case that the more massive the star, the larger its mass-loss rate. Some of these mechanisms (e.g., continuum-driven stellar winds and eruptive mass-loss phenomena; see also Renzo et al. 2020a) might even occur at low metallicity.

With the above estimate and caveats, we obtain an optimistic maximum local rate of superKNe from massive collapsars of $\sim$10–100 Gpc^{-3} yr^{-1}. On the other hand, the long-GRB rate increases with redshift in rough proportion to the cosmic star formation rate (SFR $\propto (1+z)^{3.4}$ for $z \lesssim 1$; e.g., Yüksel et al. 2008), and hence the maximum rate of superKNe is larger at redshift $z \gtrsim 1$ by a factor $\sim$10 than at $z \simeq 0$, corresponding to a maximum superKN rate of $\sim$100–1000 Gpc^{-3} yr^{-1} at $z \gtrsim 1$.

The superKN rate question can also be approached from another perspective: what is the minimum birth rate of BHs in the PI mass gap to explain GW190521-like merger events (Section 5.3) via the massive collapsar channel? The rate of GW190521-like mergers at $z \simeq 0$ was estimated by LIGO/Virgo to be $\sim$0.5–1 Gpc^{-3} yr^{-1} (Abbott et al. 2020). This rate is smaller than the maximum superKN rate estimated above, consistent with only a small fraction of the BHs that are formed through this channel ending up in tight binaries that merge due to gravitational waves at $z \approx 0$.

4.2. Discovery with Optical/IR Surveys

We now evaluate the prospects for discovering superKNe in impending wide-field optical/IR surveys.

First, we explore the expected observable rates in the Legacy Survey of Space and Time (LSST), conducted with the Vera Rubin Observatory. LSST is currently set to commence in early 2024, and it will explore the southern sky in optical wavelengths to a 5σ stacked nightly visit depth of $\sim$24 mag. We inject the set of SEDONA light curves for the models described in Table 2 into the publicly available LSST operations simulator, OpSim (Delgado & Reuter 2016). We use the most recent baseline scheduler (`baseline v1.7`) to calculate the LSST pointings, limiting magnitudes, and expected sky noise across a full simulated 10 yr survey in the *ugrizY* bands. We additionally apply dust reddening, following the dust maps of Schlegel et al. (1998). For each model, we randomly inject a superKN into the full LSST simulation 300 times (including both the wide–fast–deep survey and the deep-drilling fields) at redshift bins of 0.01.

We find that the superKNe discovered in the LSST simulation are confined to the local universe, with $z < 0.1$. Assuming that the superKN rate traces star formation with a local rate of 10 Gpc^{-3}yr^{-1}, we expect LSST to discover $\sim$0–0.2 superKNe annually, resulting in up to two events over its nominal duration of 10 yr. We note that the larger the ejecta masses (i.e., Models B and E), the more likely the detection with LSST.

Given the expected red colors of the superKN emission (Figure 8), we additionally explore the possibility of discovering superKN with Roman, which is expected to launch in the mid 2020s. Although it has not yet been fully defined, Roman is expected to conduct a $\sim$5 yr, 10 deg^2 SN survey, primarily targeted at Type Ia SNe, for cosmological distance measurements. We assume a survey cadence of 30 days and a single-visit, stacked 5σ depth of 27 mag, corresponding to roughly an hour of integration time (in the F158 band). We inject the same set of models, using the Roman F062, F158, and F184 filters, corresponding to central wavelengths of 0.62, 1.58, and 1.83 μm, respectively. We assume that observations are taken via each filter in the same epoch, and consider superKNe with three or more 3σ detections to be detectable. Assuming that the Roman wide-field survey footprint will be chosen to minimize galactic dust, we do not account for any galactic reddening.

We find that the Roman simulation is most sensitive to models with the largest lanthanide fractions. Assuming that the superKN rate traces star formation with a local rate of 10 Gpc^{-3}yr^{-1}, we expect a 5 yr Roman survey, as described, to find roughly 1–20 superKNe, favoring the lanthanide-rich Model B. These superKNe will be observable out to a redshift of $z \sim 0.9$. We note that the longer cadences significantly decrease the number of superKN detections that are likely to be possible with Roman, at least using the three-detection discovery criterion that we have adopted.

4.3. Energetic Long GRBs Accompanied by SuperKNe

SuperKNe could also be detected by following a subset of long GRBs. Figure 20 summarizes the GRB properties of our fiducial massive collapsar model `250.25`. We find accretion timescales that are comparable to those of ordinary collapsars for lower-mass progenitor stars (Appendix E). These mass gap collapsars are therefore candidates that could potentially contribute to the observed population of long GRBs, except that they may be more luminous and energetic than typical GRBs by a factor of $\sim$10, if the gamma-ray luminosity tracks the BH-accreted mass. Furthermore, if the fraction of massive stars above the PI mass gap that form or evolve into collapsar progenitors is greater at lower metallicity, this could imprint itself onto the redshift evolution of the long-GRB luminosity function (for which there is claimed evidence; see Petrosian et al. 2015; Sun et al. 2015; Pescalli et al. 2016).

In the local universe, long GRBs with SNe are commonly accompanied by luminous hyperenergetic SNe Ic-bl (e.g., Woosley & Bloom 2006; Japelj et al. 2018; Modjaz et al. 2020). The superKN transients that we predict from the birth of more massive BHs have comparable or moderately lower peak luminosities than ordinary collapsar SNe (e.g., Cano 2016), but they are significantly redder (Figures 7 and 8). Luminous optical SNe have been ruled out as accompanying a few nominally long-duration GRBs (Fynbo et al. 2006; Gehrels et al. 2006). One of these events, GRB 060614, was found to exhibit a red excess that Jin et al. (2015) interpreted as a KN. However, the luminosity and timescale of the excess could also be consistent with superKN emission from a massive collapsar of the type described here. We encourage future deep IR follow-up observations of energetic long GRBs with Roman or JWST, on timescales of weeks to months after the burst, to search for IR superKN emission.

4.4. SuperKNe Embedded in AGN Disks

The optical emission from superKNe could be significantly enhanced by circumstellar interaction, if they are embedded in gas-rich environments.

Graham et al. (2020) reported a candidate optical wavelength counterpart to GW190521, in the form of a flare from an AGN. The flare reached a peak luminosity $L_{\rm pk} \sim 10^{45}$ erg s^{-1}, in excess of the nominal level of AGN emission, and lasted over a timescale $t_{\rm pk} \sim 50$ days, during which it radiated a total energy of $E_{\rm rad} \sim 10^{51}$ erg. Shibata et al. (2021) proposed the scenario of GW190521 being a massive stellar CC, generating a single BH and a massive accretion disk $\gtrsim 10$–$50 M_\odot$, rather than a binary BH merger. Although our results in Sections 5.2 and 5.3 challenge this interpretation, our present work shows that another prediction for this scenario is a superKN counterpart with $M_{\rm ej} \sim 3$–$20 M_\odot$ and $v_{\rm ej} \sim 0.1$ c. Although the predicted peak timescale—$t_{\rm pk} \sim 50$ days; Equation (28)—of the superKNe emission roughly agrees with that observed by Graham et al. (2020), the luminosity powered by radioactivity $\sim 10^{42}$ erg s^{-1} (Figure 7) is too small to explain the observations, by several orders of magnitude.

This problem could be alleviated by the collapsing star being embedded within a dense gaseous AGN disk, however (e.g., Cantiello et al. 2021; Dittmann et al. 2021; Jermyn et al. 2021). If the density of the AGN disk at the star location is sufficiently high, $\rho \gtrsim 10^{-15}$ g cm^{-3}, runaway accretion of mass might help in building up very massive and fast-rotating helium cores. The mass accretion might be interrupted as the AGN turns off (over a timescale of a few Myr) and, depending on the balance between the mass-loss processes and the previous accretion phase, one might obtain a superKN progenitor. At its collapse, a shock-mediated collision between the superKN ejecta and the surrounding disk material could power a more luminous optical signal than from radioactive decay alone, akin to interaction-powered superluminous SNe (e.g., Smith et al. 2007).

Given the large kinetic energy of the superKN ejecta, $E_{\rm kin} \sim M_{\rm ej} v_{\rm ej}^2/2 \sim 1$–$5 \times 10^{53}$ erg, the Graham et al. (2020) transient could be powered by tapping into only $\sim 1\%$ of the $E_{\rm kin}$ from shock deceleration. Insofar as such luminous shocks are radiative and momentum-conserving, the swept-up gaseous mass in the AGN disk required to dissipate $E_{\rm rad} \sim 10^{51}$ erg would only be $M_{\rm sw} \sim (E_{\rm rad}/E_{\rm kin}) M_{\rm ej} \sim 0.1$–$1 M_\odot$. Treating the swept-up material as being approximately spherical and expanding at $\sim v_{\rm ej}$, the optical diffusion time through $M_{\rm sw}$ is (Equation (28))

$$t_{\rm pk,min} \approx 5\ {\rm d} \left(\frac{M_{\rm sw}}{0.3 M_\odot}\right)^{\frac{1}{2}} \left(\frac{v_{\rm ej}}{0.1c}\right)^{-\frac{1}{2}} \left(\frac{\kappa}{0.3\ {\rm cm^2\ g^{-1}}}\right)^{\frac{1}{2}}, \quad (33)$$

where κ is now normalized to a value more appropriate to AGN disk material. Insofar as $t_{\rm pk,min}$ is significantly shorter than the observed $\sim$50 day rise time of the Graham et al. (2020) counterpart, this implies that the rise of the putative counterpart would instead need to be limited by photon diffusion through the unshocked external AGN disk material (e.g., Graham et al. 2020; Perna et al. 2021).

The bigger challenge for this scenario is the typically much closer source distance for GW190521 that would be predicted as the result of a self-gravitating collapsar disk instead of a binary BH merger (redshift $z \lesssim 0.05$; Section 5.2), compared to that of the AGN, as identified by Graham et al. (2020) at redshift $z = 0.438$.

5. Other Observable Implications

5.1. Luminous Slow Radio Transients

In addition to their prompt optical/IR signal, superKNe produce synchrotron radio emission as the ejecta decelerate, by driving a shock into the circumburst medium (e.g., Nakar & Piran 2011; Metzger & Bower 2014). This emission can be particularly luminous, because the kinetic energy of the superKN ejecta $E_{\rm kin} \approx 1$–5×10^{53} erg can be one to two orders of magnitude higher than those of ordinary collapsar SNe.

The radio transient rises on the required timescale for the ejecta to sweep up a mass comparable to their own:

$$t_{\rm radio} \approx 200\ {\rm yr} \left(\frac{E_{\rm kin}}{5 \times 10^{53}\ {\rm erg}}\right)^{\frac{1}{3}} \left(\frac{v_{\rm ej}}{0.1c}\right)^{-\frac{5}{3}} \left(\frac{n}{1\ {\rm cm^{-3}}}\right)^{-\frac{1}{3}}, \quad (34)$$

where n is the particle density of the external medium. The peak luminosity at frequency $\nu = 1$ GHz can be estimated as (e.g., Nakar & Piran 2011)

$$\nu L_\nu \approx 5 \times 10^{39}\ {\rm erg\ s^{-1}} \left(\frac{E_{\rm kin}}{5 \times 10^{53}\ {\rm erg}}\right) \left(\frac{v_{\rm ej}}{0.1c}\right)^{2.3} \times \left(\frac{n}{1\ {\rm cm^{-3}}}\right)^{0.83} \left(\frac{\epsilon_e}{0.1}\right)^{1.3} \left(\frac{\epsilon_B}{0.01}\right), \quad (35)$$

where the fractions of the shock energy that are placed into the relativistic electrons ϵ_e and the magnetic fields ϵ_B are normalized to characteristic values, respectively, and we have assumed a power-law index $p = 2.3$ for the energy distribution of the shock-accelerated electrons, $dN/dE \propto E^{-p}$.

For the characteristic circumstellar densities $n \sim 0.1$–10 cm^{-3}, the peak radio luminosity is comparable to those of rare energetic transients, such as those from binary neutron star mergers that generate stable magnetar remnants (e.g., Metzger & Bower 2014; Schroeder et al. 2020). However, the predicted timescale of the radio evolution, from decades to centuries, is much longer in the superKN case, due to the large ejecta mass. This slow evolution makes it challenging to uniquely associate the radio source with a known GRB or gravitational-wave event, or even to identify it as a transient in radio time-domain surveys (e.g., Metzger et al. 2015). We note that luminous radio point sources are in fact common in the types of dwarf galaxies that host collapsars (e.g., Eftekhari et al. 2020). Ofek (2017) places an upper limit of $\mathcal{N} \lesssim 5 \times 10^4$ Gpc^{-3} on the local volumetric density of persistent radio sources in dwarf galaxies of luminosity $\gtrsim 3 \times 10^{38}$ erg s^{-1}. Assuming that the superKN radio emission remains above this luminosity threshold for the time $t_{\rm det} \sim 10 t_{\rm radio} \sim 10^3$ yr, this constrains the local rate of superKNe to obeying $\lesssim$10–100 Gpc^{-3} yr^{-1}, which is consistent with the estimates given in Section 4.1.

5.2. Gravitational-wave Emission

The accretion disks formed in superKN collapsars may become susceptible to gravitational instabilities if their disk mass approaches an order-unity fraction of the BH mass during the fallback evolution process (Section 2.2). As shown in Figure 9, only progenitor cores with high angular momentum (small $r_{\rm b}$ and/or high $f_{\rm K}$) lead to fallback accretion that result in gravitational instabilities. Low–angular momentum cores form heavier BHs instead, with relatively smaller disk masses.

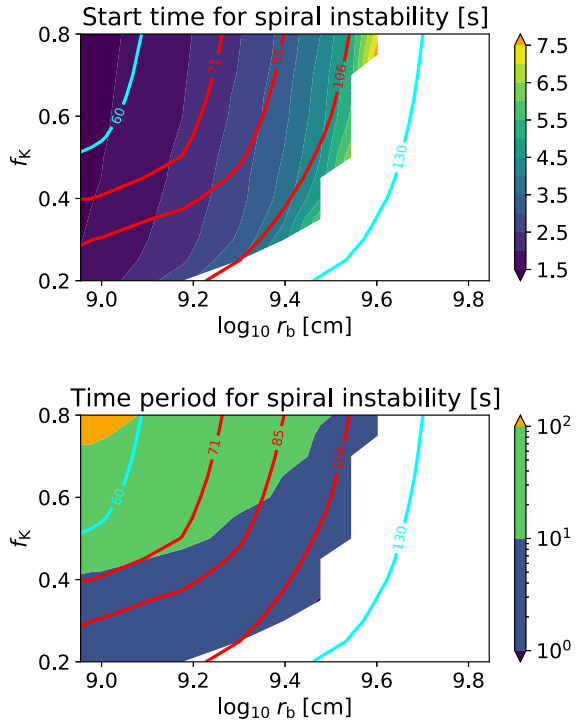

Figure 9. Time after CC at which the gravitational instabilities in the collapsar disk first set in (top panel) and the period over which the gravitational instabilities are continuously excited during the fallback process (bottom panel), shown in the space of $\{r_b, f_K\}$ for the fiducial progenitor model `250.25`, with $p = 4.5$. The white space indicates the models that do not experience gravitational instabilities during fallback accretion. The red contours indicate the inferred primary mass of GW190521 [$M_\odot$], together with its 90% confidence limits. The cyan contours delineate the final BH masses of 60 $M_\odot$ and 130 $M_\odot$, which approximately correspond to the lower and upper end of the PI mass gap.

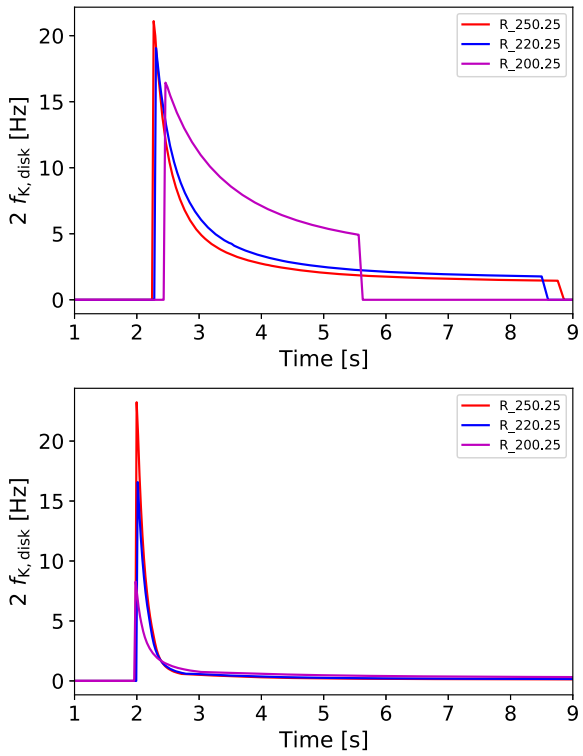

Figure 10. The disk frequency evolution (Equation (18)) for three progenitor models (`250.25`, `220.25`, and `200.25`), with rotation parameters $p = 4.5$, $r_b = 1.5 \times 10^9$ cm and an overall small ($f_K = 0.3$; top) or large ($f_K = 0.6$; bottom) Keplerian angular momentum parameter. The plots show twice the orbital angular frequency, which corresponds to the gravitational-wave frequency of the $m = 2$ density mode of the gravitationally unstable disk. The frequency evolution is largely controlled by f_K, with all models reflecting the "sad trombone" nature of the gravitational-wave signal.

The onset time of the instability, of typically a few seconds (Figure 9), which is representative of all the superKN progenitor models investigated here, is determined by the progenitor structure, its rotation profile, and the freefall timescale. Once triggered, the subsequent fallback material collapsing onto the disk continues to excite the instabilities in the collapsar disk on a timescale of seconds to hundreds of seconds (Figure 9), until the viscous draining of the disk becomes fast, compared to the freefall timescale of the remaining outer layers of the progenitor star (roughly $\sim$10 s for our fiducial model in Figure 2).

The onset of the instability manifests itself as the exponential growth of a nonaxisymmetric one-arm ($m = 1$) density mode in the disk, with a growth time on the order of the orbital period of the disk, which is typically followed by exponential growth of an $m = 2$ mode (e.g., Kiuchi et al. 2011; Shibata et al. 2021; Wessel et al. 2021). These nonaxisymmetric density perturbations give rise to gravitational-wave emission, with dominant frequencies at the orbital and twice the orbital frequency, respectively (e.g., Wessel et al. 2021).

As long as the further fallback keeps the disk in the instability regime defined by Equation (25), we assume that the dominant gravitational-wave frequencies of these modes are determined by the evolving angular frequency $\Omega_{\mathrm{K,disk}}$ of the disk (Equation (18)), with radius $r_{\mathrm{disk}}(t)$ (Section 2.2). Since $r_{\mathrm{disk}}(t)$ monotonically increases with time as the BH grows and material with a larger specific angular momentum enters the disk, the gravitational-wave frequencies decrease, sweeping down with a rate and amplitude that depend on the density and angular momentum structure of the progenitor star envelope. The gravitational-wave signal thus exhibits a "sad trombone" pattern in the time–frequency spectrogram, as opposed to the "chirp" signal that is generally associated with gravitational waves from compact binary mergers. Examples of the frequency evolution of the disk for different mass models and for the progenitor envelope with high and low specific angular momentum are shown in Figure 10. Over a large range of the parameter space, and the progenitor models explored here, superKN collapsars are strong emitters of quasi-monochromatic gravitational waves of duration $\sim$1–100 s, with a decreasing frequency trend (between $\sim$0.1–40 Hz for the $l = m = 2$ mode and $\sim$ a few $\times 10^{-2}$–25 Hz for the $l = 2$, $m = 1$ mode) that is characteristic of their progenitor stellar structure (see Figures 9 and 21 for a representative example). If detected, such gravitational-wave signals could reveal information about the rotation profiles of and angular momentum transport in evolved massive stars. The "sad trombone" feature being simultaneously followed by typically two dominant modes separated in frequency space by the instantaneous characteristic disk rotation frequency may prove useful when searching for and detecting such sources with gravitational-wave detectors.

We calculate the gravitational-wave strain of the emitted gravitational waves as described in Appendix F. Figures 11–14 present the results for the gravitational-wave emission, evaluated for a typical distance of 200 Mpc, at which superKN events are expected to occur once every $\sim$3 yr at our fiducial local superKN

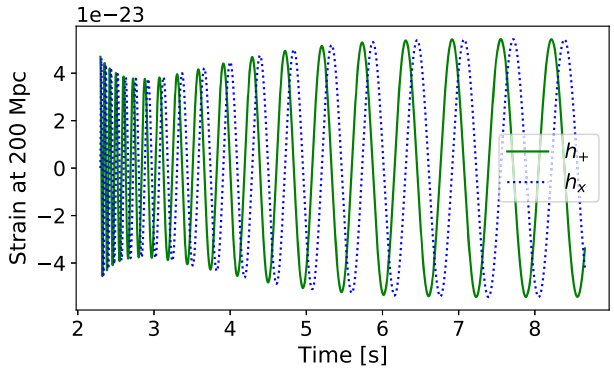

Figure 11. Plus and cross-polarization strain amplitudes of the $l = m = 2$ mode of the gravitational waves resulting from the gravitationally unstable collapsar disk in the fiducial model shown in Figure 2, with $p = 4.5$, $f_K = 0.3$, and $r_b = 1.5 \times 10^9$ cm, assuming a face-on orientation of the accretion disk ($\iota = 0$). The emission starts a few seconds after the onset of the collapse and persists for several seconds, until the viscous draining of the disk dominates the fallback accretion, with the disk becoming stable again at around 9 s after the onset of the collapse.

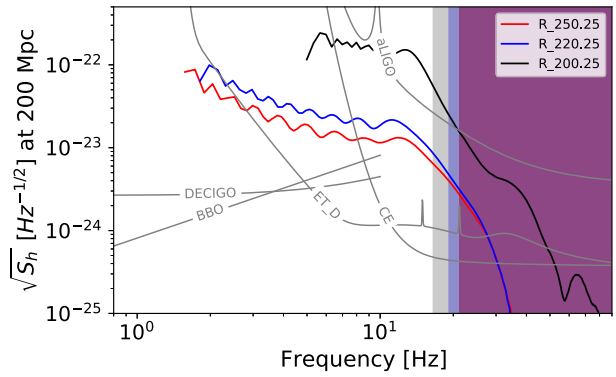

Figure 12. Amplitude spectral density of the gravitational-wave emission from the collapsar disk, shown for three progenitor models (`250.25`, `220.25`, and `200.25`) and the stellar rotation parameters $p = 4.5$, $f_K = 0.3$, and $r_b = 1.5 \times 10^9$ cm, at an assumed source distance of 200 Mpc. The shaded region for each curve shows the unphysical frequency regime above the maximum disk frequency, as plotted in Figure 10, which is ignored in the S/N calculations. Shown for comparison are the measured or predicted noise curves for aLIGO, CE, ET, DECIGO, and BBO, with sensitivity curve data from https://dcc.ligo.org/LIGO-T1500293/public and Yagi & Seto (2011).

rate of 10 Gpc^{-3} yr^{-1} (Section 4.1). Figure 11 shows the time evolution of the plus and the cross-polarization strain calculated for the fiducial progenitor model (Figure 2), assuming a face-on orientation of the collapsar disk ($\iota = 0$). The maximum characteristic strain h_c (typically, $h_c \sim 10^{-24}$–10^{-22}) and the frequency range of the gravitational-wave emission vary considerably across the $\{f_K, r_b\}$ parameter space (Figures 21 and 22; Appendix F).

SuperKN collapsars are multiband gravitational-wave sources. Figures 12 and 14 compare the gravitational-wave signal in frequency space to the sensitivities of advanced LIGO (aLIGO), the Cosmic Explorer (CE), the Einstein Telescope (ET), the DECi-hertz Interferometer Gravitational-wave Observatory (DECIGO), and the Big Bang Observer (BBO). Gravitational-wave emission typically starts at a few tens of Hz in the frequency band of aLIGO, CE, and ET, and it subsequently drifts into the decihertz regime of DECIGO and BBO as the disk expands. The relative strain amplitudes in these two different bands encode information about the total masses and the mass profiles of the progenitors (Figure 12).

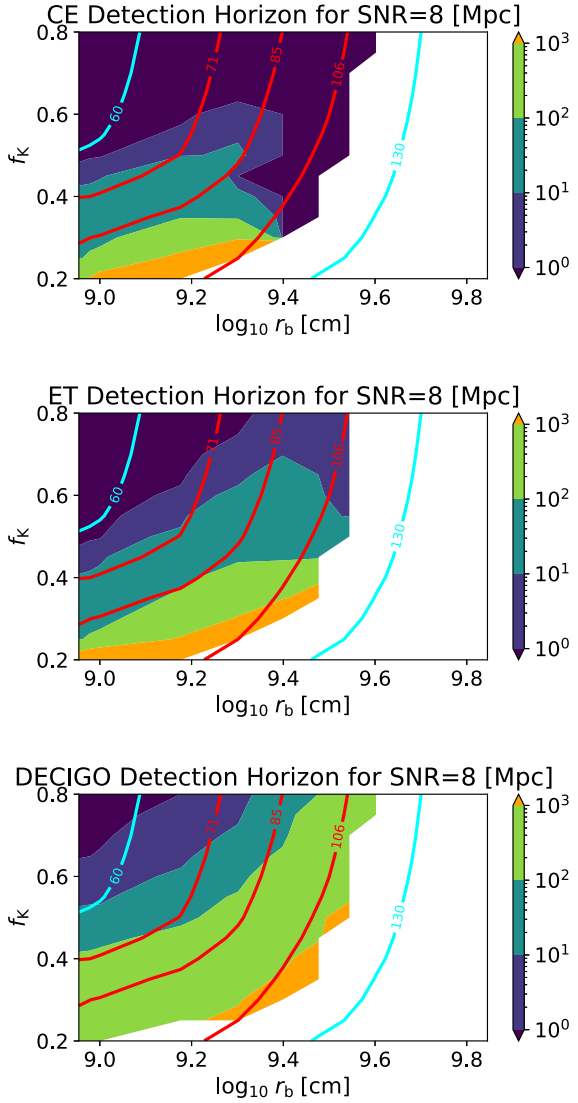

Figure 13. The detection horizons of gravitational waves from our fiducial model shown in Figure 2, with $p = 4.5$, $f_K = 0.3$, and $r_b = 1.5 \times 10^9$ cm, for CE (top), ET (center), and DECIGO (bottom), assuming optimal matched filtering and an S/N of 8. For progenitors with medium to low rotation, these detectors may be able to detect gravitational waves from superKN collapsars at distances of typically a few hundred Mpc up to a few Gpc. These estimates are based on the corresponding physical frequency regime, as indicated in Figure 10. The sharp decrease in the detection horizon for CE at $\log r_b \gtrsim 9.4$ is due to the low-frequency emission below 10 Hz (below CE's sensitivity band). The contours delineate the final BH masses, as in previous figures.

Lighter progenitors typically give rise to louder gravitational-wave signals over a narrower frequency band for the same rotation profile.

The overall magnitude of the amplitude spectral density is largely determined by the progenitor angular momentum, as illustrated in Figure 14. In the limit of high angular momentum (with a large value of the parameter f_K) for fixed r_b, the instability and gravitational-wave emission are triggered earlier than for smaller values of f_K (see Figure 9). This is because the matter deposition in the disk at early times is enhanced (instead of direct fallback onto the BH). Under these conditions, the gravitational-wave signal is relatively weak, due to the small disk and BH mass. Owing to their enhanced viscosity and enhanced accretion during the instability epoch, disks that become unstable early on tend to stay relatively light; the

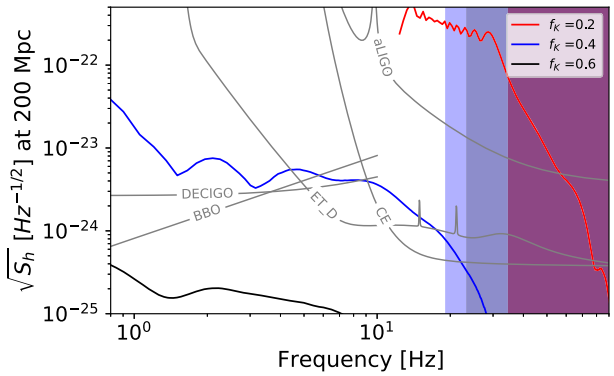

Figure 14. The same as Figure 12, but for the progenitor model `250.25`, with $p = 4.5$, $r_b = 1.5 \times 10^9$ cm, and different values of the Keplerian fraction, $f_K = 0.2$, 0.4, and 0.6. The relatively low to medium angular momentum models (here, $f_K \approx 0.2$) generate stronger signals in all detectors (detection horizon ∼400 Mpc with aLIGO at an S/N of 8), compared to cases with higher angular momentum (large values of f_K). The $f_K = 0.6$ model would only be detectable by BBO at a distance up to 100 Mpc with an S/N of 8 (see Figure 23).

gravitational-wave signal thus remains relatively weak throughout the fallback process. As a result, these signals tend to peak late, in the decihertz regime, which may only render them detectable there for Mpc distances. A nondetection in the high-frequency band may thus be indicative of the angular momentum budget of the progenitor star. In the other limit of low angular momentum (with a small value of the parameter f_K and a large r_b), the accretion disk may never become susceptible to the instability and the gravitational-wave emission may be negligible (see Figure 9). Hence, there exists an intermediate regime of progenitor angular momentum (with intermediate values of f_K), in which the gravitational-wave strain becomes maximal. For the given parameters of our fiducial progenitor model, this optimum is reached for $f_K \approx 0.2$, which is also reflected by the detection horizons (Figures 13 and 23).

We calculate a detection horizon for these events assuming an optimal matched filter and a signal-to-noise ratio (S/N) of 8 (see Appendix F for details). We find detection horizons of ∼5 Mpc (aLIGO), ∼300 Mpc (ET), ∼250 Mpc (CE), and ∼425 Mpc (DECIGO) for our fiducial model with mass $250.25 M_\odot$, $f_K = 0.3$, and $r_b = 1.5 \times 10^9$ cm. A parameter space study of the detection horizons is presented in Figure 13, showing that third-generation detectors (ET and CE), as well as DECIGO, are able to detect gravitational waves from superKN collapsars at distances of typically a few hundred Mpc up to a few Gpc. The detection horizons for aLIGO are typically limited to $\lesssim$100 Mpc (Figure 23; Appendix F). BBO will be particularly sensitive to the lowest-frequency sources with low angular momentum in the progenitor "core" (medium to large values of r_b), and typically reach several hundred Mpc to several Gpc (Figure 23; Appendix F).

5.3. GW190521

Our work has several potential implications for the gravitational-wave event GW190521 (Abbott et al. 2020). First, as already discussed, in the standard interpretation of GW190521 as a binary BH coalescence, the mass loss associated with the birth of one or both of the constituent BHs can place them in the nominal PI mass gap "from above," even if they would have been above the PI gap if all of the star's mass had been accreted at the time of CC (Figure 4, top panel). Generating a BH with a mass consistent with the more massive member of GW190521, of $\sim 88 M_\odot$ (Abbott et al. 2020), from a star with a helium core nominally above the gap, would require the ejection of $\gtrsim 50 M_\odot$ of ejecta (most of it r-process-enriched; Section 2.2). In a direct sense, superKNe probe one channel for the forming of BHs in the PI mass gap.

Our scenario requires a fast-rotating precollapse star, and predicts that the magnitude of the BH spin would be nearly maximal ($a_{\rm BH,fin} \sim 1$; Figure 20, bottom panel). Although a low orbit-aligned spin $\chi_{\rm eff} \lesssim 0.35$ (90% confidence) was measured for GW190521, there is some evidence for a large spin component in the binary plane (Abbott et al. 2020). However, assuming that progenitor stars can retain large rotation rates (see, however, Spruit 2002; Fuller & Ma 2019), and that the progenitor of GW190521 was formed from an isolated stellar binary through common envelope evolution (e.g., Belczynski et al. 2016), through stable mass transfer (e.g., van den Heuvel et al. 2017; van Son et al. 2022), or through chemically homogeneous evolution driven by tidal interactions (e.g., Maeder & Meynet 2000; de Mink & Mandel 2016; Marchant et al. 2016), one would expect the stellar angular momentum vector—and hence those of the BHs formed from the collapse—to be aligned with the orbital angular momentum (Mandel & de Mink 2016).

In the case of rapidly rotating progenitors, we speculate that misaligned spins could arise from a kick imparted to the BH by mass loss in the disk winds. Our calculations in Section 5.2 indicate that the formed disks can become self-gravitating, and hence they will become subject to bar-mode-like instabilities, generating nonaxisymmetric spiral density waves. The latter could impart a nonaxisymmetric component on the wind mass loss, which would endow the BH with an effective kick. To significantly misalign the spins without breaking the binary, the natal kick must be comparable to the precollapse orbital velocity of the system, $v_{\rm kick} \sim 300$ km s^{-1} (e.g., Kalogera 1996; Callister et al. 2021). Given the characteristic wind ejecta speed $v_{\rm ej} \sim 0.1$ c, from momentum conservation an asymmetry in the disk mass-loss rate or velocity at the level of $\gtrsim v_{\rm kick}/v_{\rm ej} \sim 10^{-2}$ would be sufficient to impart significant spin–orbital misalignment. Although self-gravitating instabilities result in nonaxisymmetric disk density fluctuations at the level $\delta\rho/\rho \gtrsim 0.1$, quantifying the extent to which these impart nonaxisymmetric mass loss will require additional GRMHD simulations of disk outflows in the regime of massive self-gravitating disks.

In an alternative approach, Shibata et al. (2021) interpret GW190521 in terms of gravitational waves from a nonaxisymmetric instability similar to those discussed in Section 5.2, in a massive BH–disk system, thought to originate from the collapse of a massive star. In contrast to the BH–torus systems of fixed mass that have been numerically evolved by Shibata et al. (2021), however, mass is continuously fed to the disk at a rate $\dot{m}_{\rm fb,disk}$ in an astrophysical setting, due to the fallback of the progenitor envelope (Section 2.2). If the accretion disk approaches the gravitationally unstable regime, its mass evolution $M_{\rm disk}(t)$ is dominated by the addition of fallback material through $\dot{m}_{\rm fb,disk}$. The associated timescale over which the fallback rate changes is $\tau_{\dot{m}_{\rm fb,disk}} \propto t^\alpha$, where $\alpha \approx 1$ (Siegel et al. 2019 and Section 2.2). This is reflected by the fact that the disks for the progenitor models considered here become gravitationally unstable on a timescale of a few seconds after BH formation, with this instability phase then lasting for a few

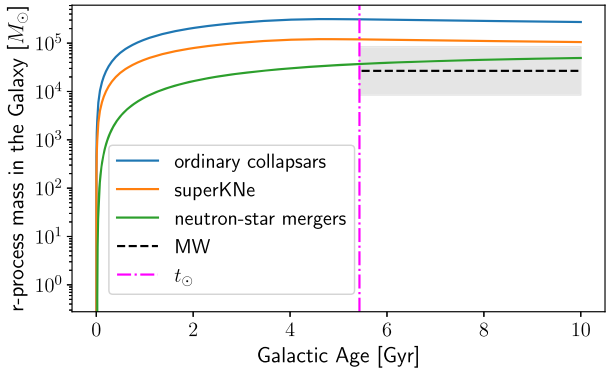

Figure 15. A one-zone chemical evolution calculation showing the contribution to the total Galactic *r*-process content (stars and interstellar medium gas) from superKNe relative to ordinary collapsars and neutron star mergers as a function of Galactic age. The underlying model and parameters for neutron star mergers as well as ordinary collapsars are as in Siegel (2019; see their Methods and Extended Data in Figures 9 and 10), except for an updated local neutron star merger rate of $\sim$300 Gpc^{-3}yr^{-1} (The LIGO Scientific Collaboration et al. 2021) and an efficiency factor $f_{\rm NS} = 1$. SuperKNe are assumed to follow the cosmic SFR, with the same cutoff distribution at high metallicities as long GRBs (ordinary collapsars; see Siegel 2019 for details), corresponding to our fiducial local rate of 10 Gpc^{-3} yr^{-1} in the absence of a cutoff. We assume a moderate average yield of 5 $M_\odot$ of *r*-process material per superKN event. As a result of the cutoff and Galactic outflows, the cumulative collapsar and superKN contribution decreases slightly at late times. The horizontal dashed line and the gray shaded area ($\pm$0.5 dex) indicate an estimate of the total present-day Galactic *r*-process content, assuming that the solar abundance pattern ($A \geqslant 69$) generalizes to the entire Galactic stellar and gas mass of $\approx 6.6 \times 10^{10} M_\odot$ (McMillan 2017). The vertical dotted–dashed line indicates the time of formation of the solar system.

seconds to tens of seconds (Figure 9; Section 5.2). Generating a gravitational-wave signal of only a few cycles and duration $t_{\rm GW} \sim 0.1$ s, as required by GW190521 (Abbott et al. 2020), with comparatively negligible amplitude thereafter, thus requires a fallback rate—given by the total mass of the BH–disk system divided by the duration of the signal of $\dot{m}_{\rm fb,disk} > (M_\bullet + M_{\rm disk})/t_{\rm GW} \sim 650$–$1000\, M_\odot\ {\rm s}^{-1}$—for the configurations considered by Shibata et al. (2021). While fallback rates of the order of up to ~ 30–$40\, M_\odot\ {\rm s}^{-1}$ may be realistically reached (see, e.g., Figure 2), fallback rates that are larger by one or two orders of magnitude seem implausible, even with the most compact progenitor models possible (Section 2.1). These fallback rates also set limits on the compactness, and thus also on the gravitational-wave frequency, of possible BH–disk systems—the frequency of the gravitational-wave emission may be in tension with GW190521 as well. While a frequency around ~ 60 Hz for GW190521 may not be impossible, per se, our unstable BH–disk systems are typically not compact enough to reach such high frequencies, even for the $l = m = 2$ mode, and they instead strongly prefer maximum frequencies below 20–30 Hz (Figure 10). Much closer detection horizons are another consequence of the weaker gravitational-wave signals that we predict from massive collapsars, which amount to $\lesssim$100 Mpc for aLIGO at O3 sensitivity (Figure 23; Appendix F); it is unlikely that a superKN transient from GW190521 would have gone undetected by existing wide-field optical surveys at such close distances.

5.4. Implications for Galactic r-Process Enrichment

Although the massive collapsars studied here are probably less common by a factor of $\lesssim$0.1–0.3 than the bulk of ordinary collapsars (Section 4.1), they can in principle generate up to $\sim$10 times more *r*-process ejecta mass for a similar progenitor angular momentum structure. The contribution of superKNe to the total *r*-process production in the Universe could therefore be non-negligible relative to that of ordinary collapsars. We illustrate this point with a one-zone chemical evolution model calculation in Figure 15, which extends the framework presented in Siegel et al. (2019). The optimistic contribution of the superKNe shown here likely represents an upper bound, given the uncertainties and caveats discussed in Section 4.1 and the fact that we applied a rather optimistic metallicity cutoff identical to that for low-mass collapsars (long GRBs). The yield calculation in Figure 15 is meant to illustrate the *relative* contributions of the different enrichment sources. The fact that all sources overestimate to some degree the absolute total Galactic *r*-process content is of less concern; addressing this issue would require more detailed chemical evolution models beyond a one-zone approach, better taking into account the hierarchical formation history of the Milky Way, Galactic inflows and outflows, metallicity-dependent cutoffs, detailed yield distributions for source populations, etc.

SuperKNe are probably too rare to explain the occurrence of individual *r*-process pollution events in small dwarf galaxies (e.g., Ji et al. 2016), but this does not exclude them from contributing to larger stellar systems. The total mass of the *r*-process elements in the Milky Way is only $\sim 10^4 M_\odot$, so given an *r*-process yield of $\gtrsim 10 M_\odot$ per superKNe, the number of contributing events must be $\lesssim$1000, and probably $\lesssim$100 (accounting for the dominant contributions likely coming from other channels, such as lower-mass collapsars and neutron star mergers).

Depending on the efficiency of the gas mixing and retention in the environments of superKNe, subsequent generations of star formation could produce a modest number of extremely *r*-process-enriched stars. The dilution mass of the interstellar medium into which the superKN ejecta is mixed can be estimated as (e.g., Macias & Ramirez-Ruiz 2019)

$$M_{\rm dil} \approx 2 \times 10^7 M_\odot \left(\frac{E_{\rm kin}}{5 \times 10^{53} {\rm erg}}\right)^{0.97} \left(\frac{n}{{\rm cm}^{-3}}\right)^{-0.062}, \quad (36)$$

where we have assumed 10 km s^{-1} for the sound speed of the interstellar medium. The value of $M_{\rm dil}$ in superKNe is larger than that in ordinary SNe ($E_{\rm kin} \sim 10^{51}$ erg) or ordinary collapsars ($E_{\rm kin} \sim 10^{52}$ erg), by a factor of $\gtrsim$10–100.

The total amount of *r*-process material generated by superKNe is larger than that generated by ordinary collapsars by a similar factor of $\sim$10, while their production ~ 0.1–$0.5 M_\odot$ of ^{56}Ni and hence ^{56}Fe (Figure 5) is similar to that of ordinary collapsars. If a superKN were to occur in otherwise pristine material at very low metallicity (perhaps a questionable idealization, given that SNe tend to be spatially and temporally clustered), the next generation of stars that form from this material could possess a metallicity as low as [Fe/H] ~ -5 and a Europium abundance as high as [Eu/Fe] $\sim$5, much higher than the current record holder (Cain et al. 2020). This abundance combination would also contrast strongly with the chemical signatures of PI SNe (e.g., Woosley et al. 2002; Aoki et al. 2014), for which a large quantity of iron group elements, but no *r*-process elements, are produced.

6. Conclusions

We have explored the collapse of very massive $\gtrsim 130 M_{\odot}$ rotating helium stars and predicted their nucleosynthetic, electromagnetic, and gravitational-wave signatures. Our conclusions can be summarized as follows.

1. Building on Siegel et al. (2019), we present a semi-analytic model for the BH accretion disk in collapsars and its associated outflows that predicts the quantity and composition of the disk wind ejecta, as well as the final BH mass and spin, given an assumed angular momentum structure of the progenitor star. The accretion regimes are calibrated based on the results of numerical GRMHD simulations and analytic scaling relations (Appendix A). Although the radial angular momentum structure of the progenitor star at collapse is uncertain theoretically, our approach allows us to cover a wide portion of the physically allowed parameter space. When it is applied to "ordinary" low-mass collapsars, the model predicts accretion luminosities and durations that are broadly consistent with long-GRB observations.
2. Our main application is to massive collapsars, originating from progenitor stars with final helium core masses ~ 125–$150 M_{\odot}$, which avoid pair-instability SNe and nominally (in the case of zero mass ejection) would create BHs above the PI mass gap. Analogous to lower-mass collapsars, as the fallback accretion rate declines over time, the composition of the disk outflows systematically evolves, from heavier to lighter elements (Figure 3). Across a wide parameter space of progenitor rotational properties, we find total wind ejecta masses ~ 10–$50 M_{\odot}$, with $\sim$10%–60% being composed of r-process nuclei, including a sizable quantity of lanthanide elements that are associated with the main r-process production. The remaining ejecta are primarily unprocessed material (assumed to be ^{4}He in our models) and a modest quantity ~ 0.1–$1 M_{\odot}$ of ^{56}Ni, formed from the brief, hot, proton-rich phases of the disk evolution.
3. The radioactive decay of the r-process nuclei and ^{56}Ni in the ejecta of massive collapsars powers a months-long transient with a peak luminosity $\sim 10^{42}$ erg s^{-1} (Figure 7), which we refer to as a "superKN." The spectral energy distributions of superKNe near maximum light peak at several microns, due to the large opacity of the lanthanide elements (Figure 8), similar to lanthanide-rich KNe from neutron star mergers. Although the bolometric light curves of superKNe are broadly similar to common types of CCSNe, their combination of extremely red colors and high-velocity spectral features ($v_{\rm ej} \sim 0.1$ c) should render the superKNe distinguishable from other transient classes.

   Our radiative transfer calculations have assumed a homogeneous ejecta structure; if the ejecta instead exhibit significant radial stratification, particularly a low lanthanide abundance in the highest-velocity outermost layers, then the early light curve could be substantially brighter and bluer than our baseline predictions.
4. Even for progenitor stars well above the PI mass gap at collapse, the final BH remnant can populate the entire mass gap between ~ 55 and $130 M_{\odot}$, due to disk wind mass loss (e.g., Figure 4; Table 1). SuperKNe therefore probe one mechanism for populating the PI mass gap "from above." The BHs that are formed through this channel are predicted to be rapidly spinning, due to the large accretion of angular momentum, with a final Kerr parameter $a_{\rm BH,fin} \sim 1$. If the BH is formed in a binary, we speculate that its spin angular momentum axis could become misaligned with that of the binary angular momentum, due to nonaxisymmetric mass outflows that are associated with the gravitationally unstable phases of the accretion (Section 5.2). Future numerical simulation work will be necessary to explore this possibility quantitatively.
5. One avenue for discovering SuperKNe is via wide-field optical/IR surveys. A 5 yr survey with Roman, similar to that planned for Type Ia SNe, could potentially detect $\sim$1–20 superKNe out to redshift $z \simeq 1$, at an assumed $z = 0$ superKN rate of ~ 10 Gpc^{-3} yr^{-1}. SuperKNe could also be discovered by LSST, but the detection rate would be lower, because the predicted emission peaks at redder wavelengths than are covered by the LSST bands. Measurements or limits on the occurrence rate of superKNe would constrain the birth rate of PI mass gap BHs via this channel (for comparison, the local rate of GW190521-like mergers is ~ 1 Gpc^{-3} yr^{-1}; Abbott et al. 2020). SuperKNe may also be detectable with JWST following (particularly energetic) GRBs, after the GRB afterglow has faded.
6. The large kinetic energies of the superKN ejecta $\gtrsim 10^{53}$ erg result in a bright, long-lived synchrotron radio transient, as the ejecta decelerate via shock interaction with the circumstellar medium (Section 5.1). However, the slow evolution of the radio emission for typical circumstellar densities will render these radio sources challenging to identify as radio transients (they may appear as luminous persistent sources in star-forming dwarf galaxies, for example; Eftekhari et al. 2020).

   If superKNe occur inside gaseous AGN disks, the shock interaction with the dense disk material could substantially enhance the optical luminosity of the event relative to that powered by radioactivity alone. This offers a speculative explanation for the claimed optical counterpart of GW190521 (Graham et al. 2020), provided that it represents a gravitational-wave burst from a CC event (Shibata et al. 2021), instead of a BH merger (however, see Section 5.3).
7. The massive accretion disks from massive collapsars can become gravitationally unstable, generating gravitational-wave emission as a result of nonaxisymmetric density fluctuations. The predicted durations of the gravitational waves are several seconds or longer (calling into question the CC origin for GW190521 proposed by Shibata et al. 2021; Section 5.3), while the frequency range overlaps with the sensitivity windows of ground-based (e.g., LIGO/CE/ET) and space-based intermediate-frequency gravitational-wave detectors (e.g., DECIGO and BBO). Unlike the gravitational-wave signals of compact binary mergers, which increase in frequency and amplitude with time ("chirp"), the gravitational-wave signals of collapsar disks *decrease* in frequency as the disk radius grows ("sad trombone"). Our simple estimates suggest that gravitational waves from massive collapsar disks are detectable by CE/ET/DECIGO to distances of up to several hundred Mpc (Figures 12, 13, and 14), in which the event rate could be as high as once every few years.

8. At the optimistic maximum local rate, SuperKNe could, in principle, contribute significantly to the total production of *r*-process elements in the Universe, compared to neutron star mergers or ordinary low-mass collapsars (see Figure 15). However, given the uncertainties on the formation rates of such massive helium cores, it is unlikely that they do so (see the discussions in Sections 4.1 and 5.4). Their extremely *r*-process-rich but iron-poor ejecta could in principle seed the creation of a small fraction of stars with abundance ratios that are more extreme than the currently known metal-poor *r*-process-enhanced stars (e.g., [Eu/Fe] ∼5).

D.M.S. and A.A. acknowledge discussions with R. Essick. This research was enabled in part by support provided by SciNet (www.scinethpc.ca) and Compute Canada (www.computecanada.ca). This research was undertaken thanks in part to funding from the Canada First Research Excellence Fund through the Arthur B. McDonald Canadian Astroparticle Physics Research Institute. D. M.S. acknowledges the support of the Natural Sciences and Engineering Research Council of Canada (NSERC), funding reference number RGPIN-2019-04684. Research at the Perimeter Institute is supported in part by the Government of Canada, through the Department of Innovation, Science and Economic Development Canada, and by the Province of Ontario, through the Ministry of Colleges and Universities. A.A. acknowledges support through a MITACS Globalink Graduate Fellowship. J.B., B.D.M., and M.R. acknowledge support from the National Science Foundation (grant AST-2002577). V.A.V. acknowledges support from the Simons Foundation through a Simons Junior Fellowship (#718240) during the early phases of this project.

Data Availability: The precollapse stellar models from Renzo et al. (2020b) and Heger et al. (2000) are available at DOI: 10.5281/zenodo.3406357 and https://2sn.org/stellarevolution/rotation/, respectively. The data from our model runs, together with the visualization scripts, are available at DOI:10.5281/zenodo.5639697.

Appendix A
Dependence of Critical Accretion Rates on BH Mass

Here we estimate the various critical accretion rates that enter our calculations in Section 2.2. We focus on deriving the scaling laws as a function of the effective α viscosity parameter and the BH mass $M_\bullet$, normalizing our final results to those obtained by one-dimensional (e.g., Chen & Beloborodov 2007) and three-dimensional MHD simulations (e.g., De & Siegel 2020).

A.1. Ignition Accretion Rate

We begin with the critical accretion rate $\dot{M}_{\rm ign}$, below which neutrinos can no longer efficiently cool the inner regions of the disk, leading to its self-neutronization.

At the transition between efficient neutrino cooling and adiabatic evolution, the midplane temperature T is determined by balancing the specific rate of neutrino cooling $\dot{q}_\nu \propto T^6$ in the optically thin limit (due to the capture of relativistic electrons and positrons on free nuclei; e.g., Qian & Woosley 1996; Di Matteo et al. 2002) with the rate of viscous heating:

$$\dot{q}_{\rm visc} \approx \frac{9}{4} m_{\rm p} \nu \Omega^2 \approx \frac{9}{4} \alpha m_{\rm p} r^2 \Omega^3 \left(\frac{H}{r}\right)^2, \tag{A1}$$

where $\nu = \alpha c_{\rm s} H \simeq \alpha R^2 \Omega (H/r)^2$ is the kinematic viscosity and m_p is the proton mass. We have assumed a Keplerian disk with angular velocity $\Omega \simeq \Omega_{\rm K} = (G M_\bullet / r^3)^{1/2}$, midplane sound speed $c_{\rm s} = H\Omega$, and aspect ratio H/r. Since $H/r \sim \mathcal{O}(1)$, once advective cooling competes with radiative cooling (e.g., Di Matteo et al. 2002), we have $H/r \sim$ constant at the transition to an advective disk from an efficiently neutrino-cooled disk. This gives

$$T^6 \propto \alpha r^2 \Omega^3. \tag{A2}$$

We also assume that near the transition point to an advective disk, the radiation pressure dominates over the gas pressure in the disk midplane, i.e., the midplane pressure obeys $P \propto T^4$. From vertical hydrostatic equilibrium, we then have

$$\begin{aligned} \text{const.} \sim \left(\frac{H}{r}\right)^2 \approx \frac{c_{\rm s}^2}{r^2\Omega^2} \approx \frac{P/\rho}{r^2\Omega^2} \propto \frac{\alpha T^4 r}{\Omega \dot{M}} \\ \Rightarrow T^4 \propto \frac{\dot{M}\Omega}{\alpha r}, \end{aligned} \tag{A3}$$

where ρ is the midplane density and we have used in the final line the fact that the local disk mass $M_{\rm d} \propto \rho r^2 H$ accretes on the local viscous time $t_{\rm visc} \propto \nu/r \sim \alpha^{-1}\Omega^2 (H/r)^{-2}$, i.e.,

$$\begin{aligned} \dot{M} \propto \frac{M_{\rm d}}{t_{\rm visc}} \propto \frac{\rho r^2 H}{\alpha^{-1}\Omega^{-1}(H/r)^{-2}} \propto \alpha \rho \Omega r^3 \left(\frac{H}{r}\right)^3 \\ \Rightarrow \rho \propto \frac{\dot{M}}{\alpha \Omega r^3}. \end{aligned} \tag{A4}$$

Combining Equations (A2) and (A3), we obtain

$$\dot{M} \propto \alpha^{5/3} r^{7/3} \Omega. \tag{A5}$$

Scaling r to the radius of the ISCO, $r_{\rm ISCO} \propto M_\bullet$, we have $r \propto M_\bullet$ and $\Omega \propto M_\bullet^{-1}$, thus giving

$$\dot{M}_{\rm ign} \propto \alpha^{5/3} M_\bullet^{4/3}. \tag{A6}$$

A derivation of this scaling in the general relativistic context is given in De & Siegel (2020). The scaling $\dot{M}_{\rm ign} \propto \alpha^{5/3}$ has been verified in one-dimensional models (Chen & Beloborodov 2007) for BH masses $M_\bullet \approx 3 M_\odot$. However, the scaling should hold for the higher values of $M_\bullet$ of interest in this paper, because the assumptions that enter the above derivation (i.e., optically thin cooling and radiation pressure dominating over gas pressure at the advective transition) only strengthen with increasing BH mass. In particular, the ratio of radiation to gas pressure,

$$\left.\frac{T^3}{\rho}\right|_{\dot{M}_{\rm ign}} \propto r^{5/3}\Omega^{3/2} \propto M_\bullet^{1/6}, \tag{A7}$$

increases with $M_\bullet$. Other forms of neutrino cooling, particularly arising from the annihilation of electron–positron pairs into neutrino–antineutrino pairs, will dominate over the pair-capture rates entering the radiative cooling rate at sufficiently high T^3/ρ (e.g., Qian & Woosley 1996), changing the above scalings. However, the weak $M_\bullet$ dependence in Equation (A7) suggests that this is not likely to occur for even the highest BH masses $M_\bullet \sim 100 M_\odot$ of interest in this paper.

A.2. Neutrino Opaque and Trapping Thresholds

We now consider the accretion rate $\dot{M}_{\nu,\mathrm{r-p}}$ above which the inner disk is optically thick to neutrinos. The vertical optical depth through the disk obeys

$$\tau_\nu \propto \Sigma\kappa \propto \rho H T^2, \tag{A8}$$

where $\sigma \propto T^2$ is the energy-dependent absorption cross section with which electron neutrinos or antineutrinos are absorbed by free neutrons or protons, respectively. Using Equations (A3) and (A4) for T and ρ, and again taking $H/r \sim$ const., we find

$$\tau_\nu \propto \frac{\dot{M}^{3/2}}{\alpha^{3/2}\Omega^{1/2}r^{5/2}}. \tag{A9}$$

Evaluating the marginally thick condition $\tau_\nu = 1$ at $r \approx r_{\mathrm{ISCO}}$, we obtain

$$\dot{M}_{\nu,\mathrm{r-p}} \propto \alpha M_\bullet^{4/3}. \tag{A10}$$

A.3. Neutrino Trapping Threshold

Finally, consider the "trapping" accretion rate $\dot{M}_{\mathrm{tr}}$, above which the thermal energy released by the accretion flow is advected into the BH faster than it can be radiated through neutrinos. Equating the neutrino diffusion timescale out of the disk midplane $t_{\mathrm{diff}} \sim \tau_\nu(H/c)$ with the inward flow time $\sim r/v$, we find that the neutrinos are trapped for $\tau_\nu > (c/v)(r/H)$. Using $v \sim \nu/r$ for the inflow velocity of a steady disk and Equation (A8), and again taking $H/r \sim$ const., the trapping condition can be written as

$$\Sigma\nu T^2 > r. \tag{A11}$$

Finally, recalling that $\nu\Sigma \propto \dot{M}$ for steady accretion, then using Equation (A3) and evaluating Equation (A11) at $r = r_{\mathrm{ISCO}}$, we find that

$$\dot{M}_{\mathrm{tr}} \propto \alpha^{1/3} M_\bullet^{4/3}. \tag{A12}$$

Appendix B
Production of ^{56}Ni in Disk Winds and Dissociation Threshold

Assuming that the dominant seed particle formation process in the disk wind outflow is ^{4}He(2 α, γ)^{12}C, rather than the neutron-catalyzed reaction ^{4}He(αn, γ)^9 Be(α, n)^{12}C in neutron-rich environments $Y_e \ll 0.5$ (Woosley & Hoffman 1992), the destruction of α-particles in disk winds proceeds as (Roberts et al. 2010)

$$\frac{dY_\alpha}{d\tau} \approx -14\rho^2 Y_\alpha^3 \lambda_{3\alpha}, \tag{B1}$$

where Y_α is the abundance of α-particles, $\lambda_{3\alpha}(T)$ is the temperature-dependent triple-α rate coefficient, and the factor of 14 is due to assuming that α-captures cease at ^{56}Ni. Furthermore, $d\tau = -(\tau_{\mathrm{d}}/3T)dT$, where τ_{d} is the expansion time of the outflow around the point of α-particle formation. We take $\tau_{\mathrm{d}} \approx 5$–$30$ ms, which is typical of the expansion timescales for such accretion disk winds (Siegel & Metzger 2018; Siegel et al. 2019). The integration of Equation (B1) yields the resulting abundance of seed particles (Roberts et al. 2010):

$$Y_{\mathrm{seed}} = \frac{1}{56}\{1 - [1 + 35(\tau_{\mathrm{d}}/\mathrm{ms})s_{\mathrm{f}}^{-2}]^{-1/2}\}. \tag{B2}$$

Here, s_{f} is the final entropy in k_{B} per baryon, which we estimate by $s_{\mathrm{f}} \approx s_{\mathrm{m}} = s_{\mathrm{m,rad}} + s_{\mathrm{m,N}}$, where

$$s_{\mathrm{m,rad}} = \frac{11\pi^2 k^3 m_{\mathrm{p}}}{45c^3\hbar^3}\frac{T_{\mathrm{m}}^3}{\rho_{\mathrm{m}}} \tag{B3}$$

$$\approx 21\left(\frac{r_{\mathrm{disk}}}{5r_{\mathrm{g}}}\right)^{-\frac{3}{8}}\left(\frac{\dot{M}}{10^{-4}M_\odot\ s^{-1}}\right)^{-\frac{1}{4}}\left(\frac{\alpha}{0.01}\right)^{\frac{1}{4}} \times \left(\frac{M_\bullet}{3M_\odot}\right)^{\frac{7}{8}}(3h_{z,\mathrm{disk}})^{\frac{9}{4}} \tag{B4}$$

is the entropy of the radiation in the disk midplane and

$$s_{\mathrm{m,N}} \approx 13.3 + \ln\left(\frac{(T_{\mathrm{m}}/1\mathrm{MeV})^{3/2}}{\rho_{\mathrm{m}}/10^7\mathrm{g\ cm^{-3}}}\right) \tag{B5}$$

is the entropy in the nonrelativistic nucleons. The disk midplane density ρ_{m} and temperature T_{m} are calculated using an α-disk model, as in Appendix A (see also Siegel et al. 2019). We translate Equation (B2) into the mass fractions $X_{^{56}\mathrm{Ni}}$ and $X_{\mathrm{He}} \approx 1 - X_{\mathrm{seed}}$, by assuming that the seed particles are mostly within the iron peak (charge numbers $24 \leqslant Z \leqslant 28$), using the nucleosynthesis results of Siegel et al. (2019).

At late times during the fallback process (low accretion rates), the accretion disk must be hot and dense enough to dissociate α-particles as well as the heavier nuclei of the infalling stellar material into individual nucleons, a requisite for the synthesis of ^{56}Ni in disk outflows. We estimate the time of this transition to a state in which the dissociation into individual nucleons becomes suppressed by considering a fluid of neutrons, protons, and α-particles with a proton fraction $Y_e = 0.5$, then determining the state in which half of the α-particles are dissociated. Assuming that nuclear statistical equilibrium holds (a good assumption, as our disk midplane temperatures typically stay above 0.5 MeV), this can be estimated from the Saha equation (Shapiro & Teukolsky 1983):

$$X_{\mathrm{nuc}}^4 = 1.57 \times 10^4 X_\alpha \rho_{\mathrm{m},10}^{-3} T_{\mathrm{m},10}^{9/2} \exp\left(-\frac{32.81}{T_{\mathrm{m},10}}\right), \tag{B6}$$

where $X_{\mathrm{nuc}} = 2X_{\mathrm{p}} = 2X_{\mathrm{n}}$ is the mass fraction of the nucleons, with $\rho_{\mathrm{m},10}$ and $T_{\mathrm{m},10}$ denoting the midplane density and temperature in 10^{10} g cm^{-3} and 10^{10} K, respectively. Expressing $X_{\mathrm{nuc}} = 1 - X_\alpha$ and setting $X_\alpha = 0.5$, Equation (B6) can be solved numerically for the transition time t_{diss} upon inserting ρ_{m} and T_{m}, as obtained from the numerical evolution of Equations (9)–(14). The time dependence of the functions ρ_{m} and T_{m} is determined by the evolution of $M_\bullet$, M_{disk}, and r_{disk}. At $t > t_{\mathrm{diss}}$, we set $Y_{\mathrm{seed}} = 0$ in Equation (B2), discarding any potential ^{56}Ni production after this time.

Appendix C
Breakout of Winds

For the disk ejecta to break out of the collapsing stellar envelope, the ram pressure $p_{\mathrm{ej}} = \rho_{\mathrm{ej}} v_{\mathrm{ej}}^2$ must be larger than the ram pressure of the fallback material $p_{\mathrm{fb}} = \rho_{\mathrm{fb}} v_{\mathrm{ff}}^2$, where $v_{\mathrm{ej}} \approx 0.1c$ is the velocity of the disk winds and

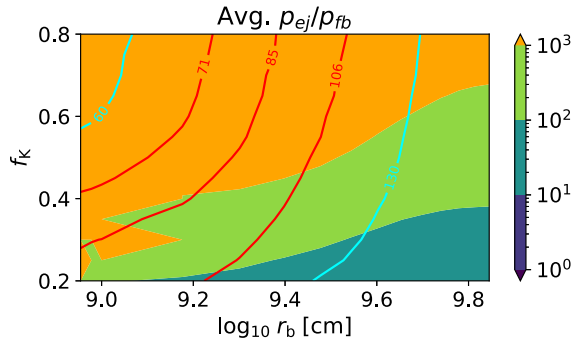

Figure 16. The average ratio of p_{ej}/p_{fb} (see Equation (C1)) during the first 100 s for model `250.25`, with $p = 4.5$ and setting $\theta_{fb} = 45°$. Disk winds can overcome the ram pressure of the infalling material in the polar directions and break out of the star, even without the help of the GRB jet.

$v_{ff} \approx \sqrt{GM_\star/r(t_s(r))}$ is the freefall velocity of the collapsing stellar material (assuming radial infall for simplicity; see Section 2.2). The density of the fallback material is determined by the mass falling onto the outflows per solid angle and per unit time, $dM_{fb}/(d\Omega dt) = \rho_{fb} r^2 v_{ff}$. We assume that the relevant fallback stream to overcome is that of material falling onto the disk within a polar angle $\theta_{fb} \approx 30°$–$45°$ and within the typical disk radius r_{disk} (Equation (19)), which we denote with $\dot{m}_{fb,disk,\theta_{fb}}$ (Section 2.2). Similarly, ρ_{ej} is determined by the wind mass-loss rate $\dot{m}_{wind}$ (Equations (20) and (13)), $d\dot{M}_{ejecta}/d\Omega = \rho_{ej} r^2 v_{ej}$. We assume that the outflows are channeled into the same solid angle within the polar angle θ_{fb}, i.e., that the angular integrated expression equals $\dot{m}_{wind}$. The relevant criterion for disk ejecta to break out of the stellar envelope is thus

$$\frac{p_{ej}}{p_{fb}} = \frac{v_{ej}}{v_{ff}} \frac{\dot{m}_{wind}}{\dot{M}_{fb,\theta_{fb}}} > 1. \quad \text{(C1)}$$

We typically find $p_{ej}/p_{fb} \gg 1$ for the models considered here (see Figure 16 for an example), showing that the outflows are indeed powerful enough to overcome the ram pressure of the infalling material. The estimate here is conservative, in the sense that it neglects the action of the GRB jet, which drills through the envelope in polar directions $\theta \lesssim 30°$, setting a pathway for the outflows to escape.

Appendix D
Resolution Studies

We have performed numerical convergence tests to check the convergence of the nucleosynthesis results from our collapsar model (Section 2.3) and to determine the optimal resolution for our numerical collapsar evolution calculations (Section 2.2). Figure 17 shows the results of two convergence tests, to determine the optimal discretization for the polar coordinate and for the time integration. The top panel illustrates that at our fiducial resolution in the polar angle of $n_\theta = 1001$, the relative error in computing the total mass of the star by numerical integration is dominated by the radial resolution of the progenitor model (relative error of $\lesssim$0.0018). The bottom panel indicates that for a sufficiently high angular resolution ($n_\theta \sim 1001$) and a sufficiently large number of time steps, of several hundred to 10^3, the relative error in computing the stellar mass by the numerical integration of Equations (9)–(14) is again dominated by the radial discretization of the progenitor model. The relative error of $\lesssim$0.002 in this case is consistent

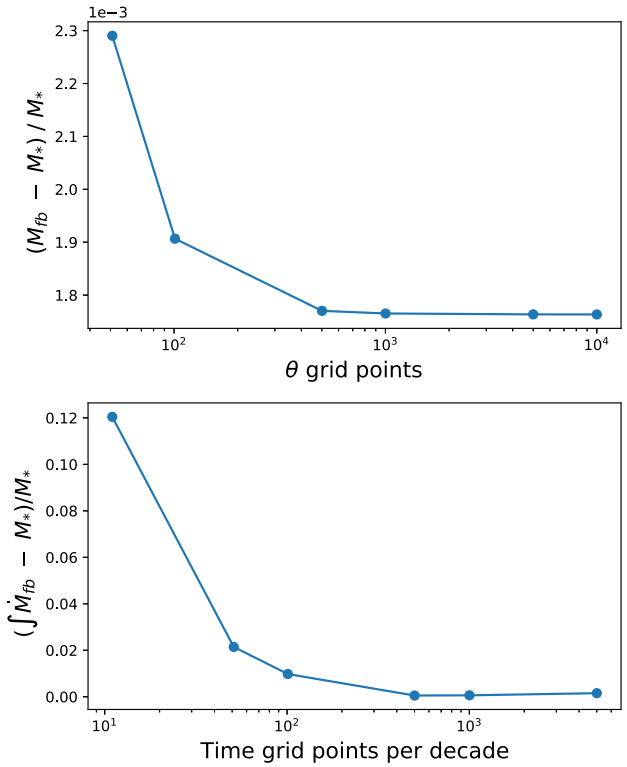

Figure 17. Convergence test for model `250.25`. Top: the relative error in computing the total mass of the star $M_\star$, using a grid discretized in both polar angle and radius, showing that at the fiducial angular resolution of $n_\theta = 1001$, the relative error $\lesssim$0.0018 is dominated by the radial resolution of the progenitor model. Bottom: the total stellar mass, as computed by the numerical integration of Equations (9)–(14) with fixed angular resolution ($n_\theta = 1001$), varying the time step. For sufficiently high temporal resolutions, the relative error of $\lesssim$0.002 is again dominated by the radial discretization of the progenitor model, consistent with the error budget shown in the top panel.

with the error budget obtained for the corresponding convergence test in the polar angle. This shows that our results are converged with roughly 10^3 grid points both in θ and in time, which we employ for all model runs.

Appendix E
Results for Ordinary Collapsars and GRB Properties

Figure 18 presents results for model `E20` of Heger et al. (2000), one representative case for ordinary collapsars below the PI BH mass gap. We vary the parameters of the adopted progenitor rotation profile (see Equation (2)) within ranges that are motivated by the structure of the stellar evolution models (see Section 2.2), making nearly identical assumptions regarding the rotation profile as for mass gap collapsars (Section 2.3.2). Our results are almost insensitive to the exact value of the power-law index p, which we thus fix to $p = 4.5$, for simplicity. For model `E20`, we find $\approx 0.04 - 0.7\,M_\odot$ of r-process material, including $\approx 0.01 - 0.04\,M_\odot$ of heavy ($A > 136$) r-process material and $\approx 0.03 - 0.65\,M_\odot$ of light ($A < 136$) r-process material, as well as $\approx 0.14 - 0.26\,M_\odot$ of ^{56}Ni.

In comparison to Siegel et al. (2019), the updated model presented here tends to predict moderately less heavy r-process material, more light r-process material, and more ^{56}Ni. This is a result of (i) a more detailed treatment of the disk accretion rate onto the BH, (ii) an additional nucleosynthesis regime of light r-process material only at high accretion rates $> \dot{M}_{\nu,r-p}$ (see Equation (26)), and (iii) a detailed evolution of the

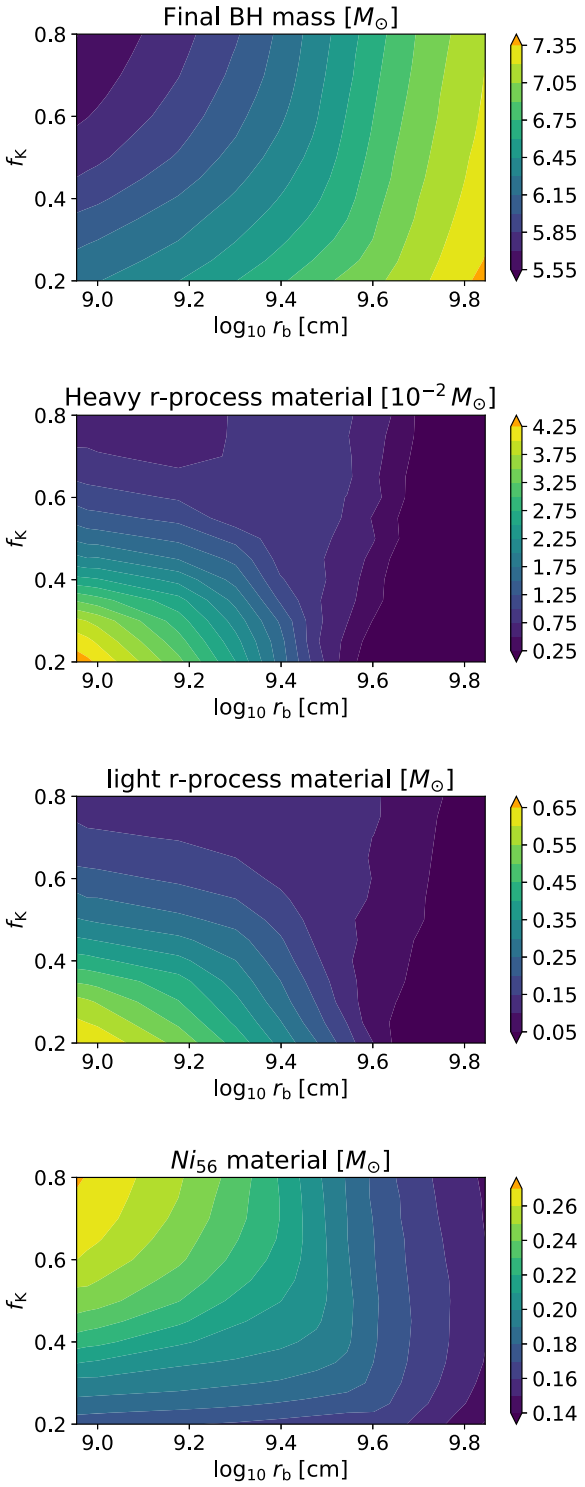

Figure 18. Scan of the parameter space for model E20 of Heger et al. (2000). The final BH mass (top) and the total ejected mass [$M_\odot$] in heavy ($A > 136$) r-process elements (center top), in light ($A < 136$) r-process elements (center bottom), and in ^{56}Ni (bottom) are shown.

nucleosynthesis regimes throughout the accretion process as a result of BH growth. Overall, however, the mass ranges of all the nucleosynthesis products found here broadly agree with those of Siegel et al. (2019). In particular, our refined analysis still predicts a sizable amount of lanthanide-bearing r-process ejecta of ≈ 0.04–$0.7\,M_\odot$ across the various progenitor models of Heger et al. (2000). These results remain consistent with Miller et al. (2020), insofar as the mass accretion and generation of disk winds occur over a wide range of accretion rates, which drift through nucleosynthesis regimes that are characterized by varying degrees of neutrino irradiation (see Equation (26)). Interestingly, our new models result in disk wind ^{56}Ni yields approaching the values required to explain the light curves of observed GRB SNe (e.g., Cano et al. 2016), without a prompt shock-heated explosion (e.g., Barnes et al. 2018) or explosive nucleosynthesis at larger radii in the disk (Zenati et al. 2020).

Our collapsar model is also in good agreement with the properties of observed GRBs. We check for the consistency of our collapsar model with observed GRBs in terms of GRB timescales and energies. We assume that the accreted mass onto the BH is proportional to the radiated gamma-ray energy, that is,

$$L_\gamma \propto \eta \dot{m}_{\rm acc} c^2, \tag{E1}$$

where L_γ is the observed gamma-ray luminosity and η is an efficiency parameter.

A necessary requirement for collapsar accretion be able to explain the observed GRBs is that the evolution time of the accretion rate should be smaller or equal to the typical time that is required to generate a GRB in the engine frame, i.e., $\tau_{\dot{m}_{\rm acc}} \lesssim \tau_{\rm GRB}$. The timescale $\tau_{\dot{m}_{\rm acc}}$ increases with time, typically expected as a power law $\tau_{\dot{m}_{\rm acc}} \propto t^\alpha$, where $\alpha \simeq 1$.[12] Following Siegel et al. (2019), we define

$$\tau_{\dot{m}_{\rm acc}} \equiv \left(\frac{{\rm d}\ln \dot{m}_{\rm acc}}{{\rm d}t} \right)^{-1}. \tag{E2}$$

Furthermore, let $t_{\rm GRB}$ denote the time relative to the onset of the disk accretion at which the equality $\tau_{\dot{m}_{\rm acc}} = \tau_{\rm GRB}$ is reached.[13] Consistency then requires

$$t_{\rm GRB} \sim \tau_{\rm GRB}. \tag{E3}$$

The GRB duration in the engine frame is determined by the condition in Equation (E4) (Bromberg et al. 2012; Sobacchi et al. 2017):

$$\tau_{\rm GRB} = \tau_\gamma + \tau_{\rm b}, \tag{E4}$$

where τ_γ is the observed duration of a GRB in the engine rest frame and $\tau_{\rm b}$ is the time required for the jet to drill through the stellar envelope. Assuming a typical value of $\tau_{\rm b} = 57^{+13}_{-10}$ s (Sobacchi et al. 2017), and a typical observed GRB duration of $\tau_\gamma = T_{90}/(1+z) = 9$ s, with a characteristic $T_{90} \simeq 27$ s and redshift $z \simeq 2$ (Narayana Bhat et al. 2016), one finds $\tau_{\rm GRB} \approx 66$ s. The top panel of Figure 19 shows that $t_{\rm GRB} \sim \tau_{\rm GRB}$ essentially throughout the parameter space. Similar results are found for the other models of Heger et al. (2000). Hence, consistency with observed GRB durations, according to Equation (E3), holds.

[12] This follows from the fact that, in an ideal accretion-powered scenario (Equation (E1)), $\tau_{\rm GRB} \propto L_\gamma/\dot{L}_\gamma \propto \dot{m}_{\rm acc}/\ddot{m}_{\rm acc} = ({\rm d}\ln \dot{m}_{\rm acc}/{\rm d}t)^{-1}$.

[13] This time ($t_{\rm GRB}$) is the maximum time over which the GRB can be accretion-powered, i.e., for which the ansatz Equation (E1) can be made. For $t > t_{\rm GRB}$, the accretion power (see Equation (E2)) fades more rapidly than the gamma-ray luminosity.

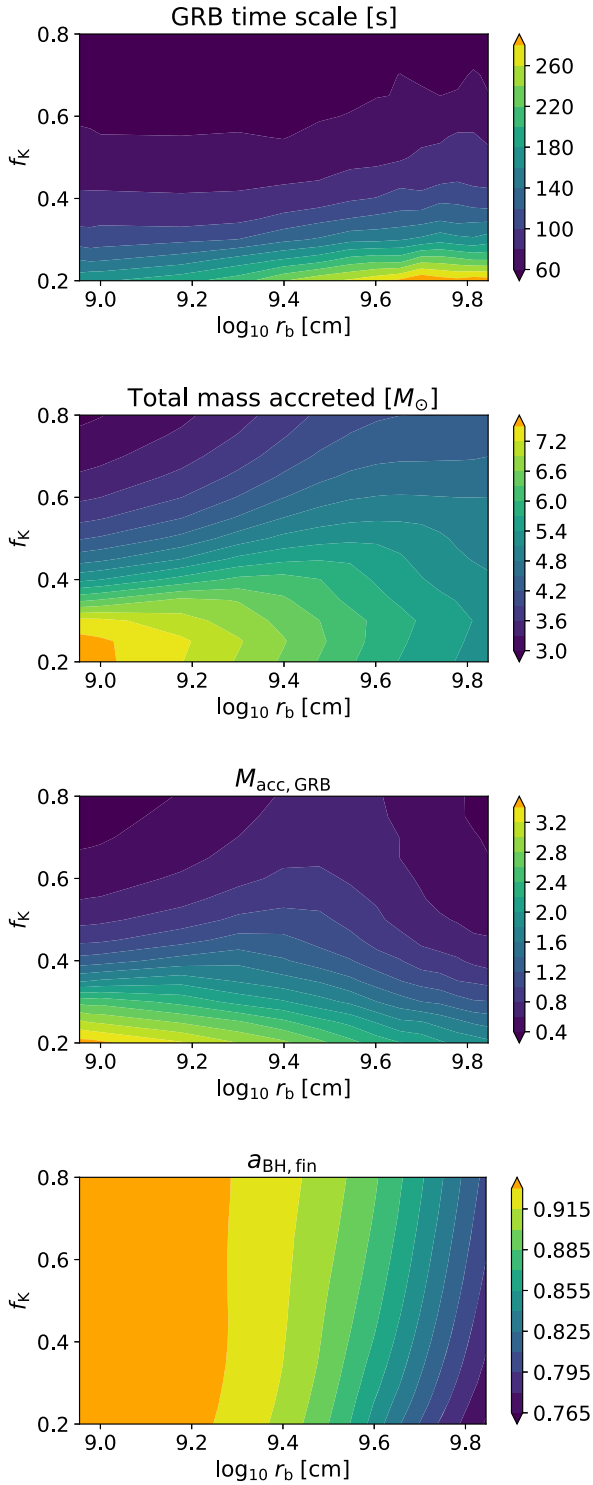

Figure 19. Scan of the parameter space for model `E20` of Heger et al. (2000). The GRB timescale $t_{\rm GRB}$ (top), the total accreted mass [$M_\odot$] (top center), the accreted mass $M_{\rm GRB}$ during the GRB phase [$M_\odot$] (bottom center), and the final dimensionless BH spin $a_{\rm BH,fin}$ (bottom) are shown.

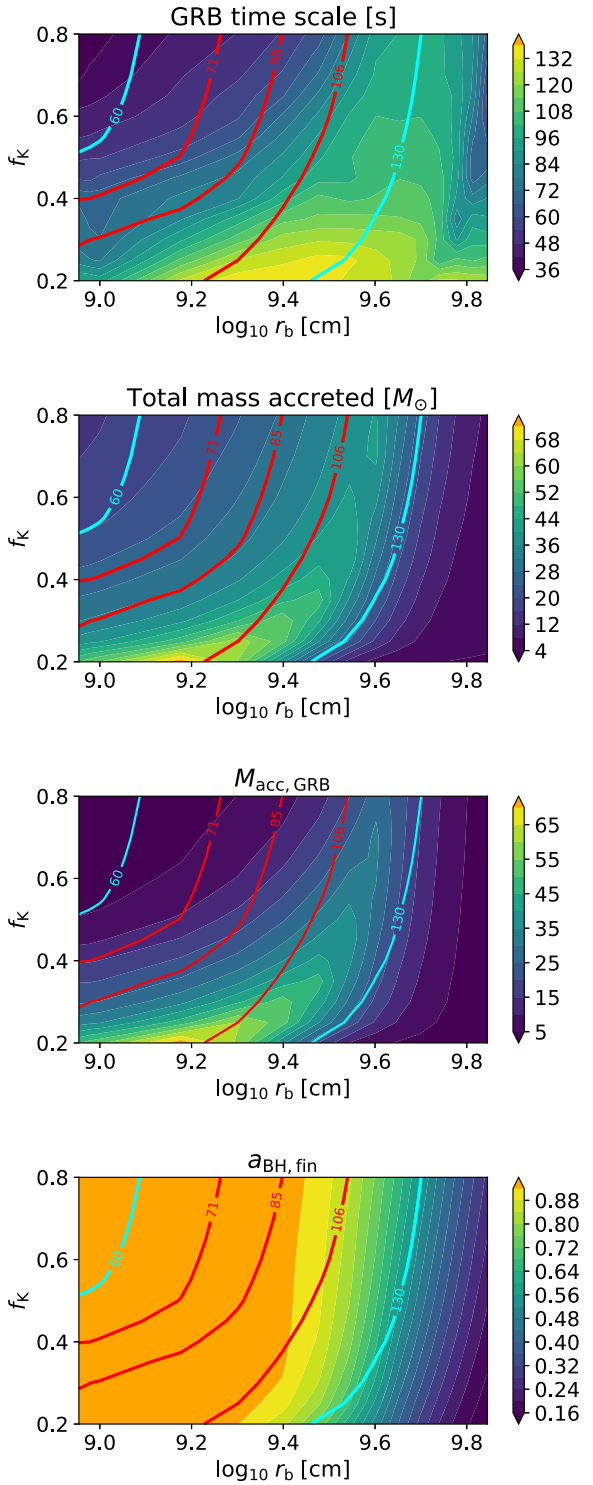

Figure 20. Scan of the parameter space for model `250.25`. The GRB timescale $t_{\rm GRB}$ (top), the total accreted mass [$M_\odot$] (center top), the accreted mass $M_{\rm GRB}$ during the GRB phase [$M_\odot$] (center bottom), and the final dimensionless BH spin $a_{\rm BH,fin}$ (bottom) are shown. The red contours indicate the inferred primary mass of GW190521 [$M_\odot$], together with its 90% confidence limits. The cyan contours delineate the final BH masses of 60 $M_\odot$ and 130 $M_\odot$, which approximately correspond to the lower and upper end of the PI mass gap.

Consistency with the typically observed GRB energies requires that

$$E_{\gamma,\rm iso} f_{\rm b} \frac{\tau_{\rm GRB}}{\tau_\gamma} \ll \int_{t_{\rm GRB}} L_{\rm jet}\, {\rm d}t < \int_{t_{\rm GRB}} \dot{m}_{\rm acc} c^2\, {\rm d}t \equiv M_{\rm acc,GRB} c^2, \quad \text{(E5)}$$

where $E_{\gamma,\rm iso} \sim 1 \times 10^{53}$ erg is the typical isotropic-equivalent gamma-ray energy of the observed GRBs, $f_{\rm b} \simeq 0.006$ is the beaming fraction (Goldstein et al. 2016), $L_{\rm jet}$ is the luminosity

of the accretion-powered jet, and $M_{\rm acc,GRB}$ is the accreted mass onto the BH through the disk over the GRB timescale $t_{\rm GRB}$. With these values, the condition translates into

$$M_{\rm acc,GRB} \gg 2.5 \times 10^{-3}\, M_\odot, \tag{E6}$$

which we find is satisfied throughout the parameter space where the peak accretion rate reaches $\dot{m}_{\rm acc} > 10^{-4}\, M_\odot\ {\rm s}^{-1}$ (see Figure 19, bottom panel), which we take as a threshold for postulating a successful jet (Section 2.2). Similar findings apply to the other models of Heger et al. (2000). We therefore find that our ordinary collapsar models are consistent with both the typical GRB duration times and energies, including drill time.

Figure 20 shows a parameter space scan for model `250.25`, a typical mass gap collapsar model. The GRB properties are in good agreement with the observational constraints. While the GRB durations are typically similar to those for ordinary collapsars, the accreted mass during the GRB phase may be up to a factor of ∼10 higher. One may thus speculate that these models give rise to GRBs that may be a factor of ∼10 more luminous or energetic, if the gamma-ray luminosity tracks the accreted mass.

Appendix F
Gravitational-wave Emission

We calculate the gravitational-wave strain of the emitted gravitational waves by approximating "the lump" of the unstable disk (assumed to correspond to an overdensity of $\delta\rho/\rho \gtrsim 0.1$; Shibata et al. 2021; Wessel et al. 2021) and the central BH as two orbiting point masses. The frequencies of the gravitational-wave emission can thus be directly predicted from the evolution of the disk angular velocity, according to the collapsar model in Section 2.2. The maximum and minimum gravitational-wave frequencies vary considerably across the $\{f_{\rm K}, r_{\rm b}\}$ parameter space (see Figure 21 for our fiducial model).

According to the quadrupole formula, assuming that the orbital radius only changes slowly with respect to the orbital frequency, the plus (h_+) and cross ($h_\times$) polarizations of the gravitational waves at the distance r and inclination ι of the disk with respect to the observer can be written as

$$h_+(t) = \frac{4G}{rc^4}\mu r_{\rm disk}^2 \Omega_{\rm K,disk}^2 \frac{1+\cos^2\iota}{2}\cos[\Phi(t)], \tag{F1}$$

$$h_\times(t) = \frac{4G}{rc^4}\mu r_{\rm disk}^2 \Omega_{\rm K,disk}^2 \cos\iota \sin[\Phi(t)], \tag{F2}$$

where $\Phi(t) \equiv \int_{t_0}^{t} 2\Omega_{\rm K,disk}(t')\mathrm{d}t'$, with $t = t_0$ denoting the start time of the gravitational instability. These expressions apply to the $l = m = 2$ mode, while $\Omega_{\rm K,disk}$ is replaced by $0.5\Omega_{\rm K,disk}$ for the $m = 1$ mode. Furthermore, $\mu = M_{\rm lump}M_\bullet/(M_{\rm lump} + M_\bullet)$ is the reduced mass of the lump–BH system, and we set $M_{\rm lump} = f_{\rm lump}M_{\rm disk}$, with $f_{\rm lump} = 0.2$. The uncertainties on the value of $f_{\rm lump}$ can be absorbed into the uncertainties on the scale height of the disk and the threshold mass fraction $f_{\rm disk,thr} \equiv M_\bullet/M_{\rm disk}$ at which gravitational instabilities set in (see Equation (25)). We neglect corrections $\propto \dot{\mu}$ to Equations (F1) and (F2), due to a time-dependent reduced mass μ as a result of accretion onto the BH, assuming that $M_\bullet$ changes only weakly over the course of the gravitational-wave emission.

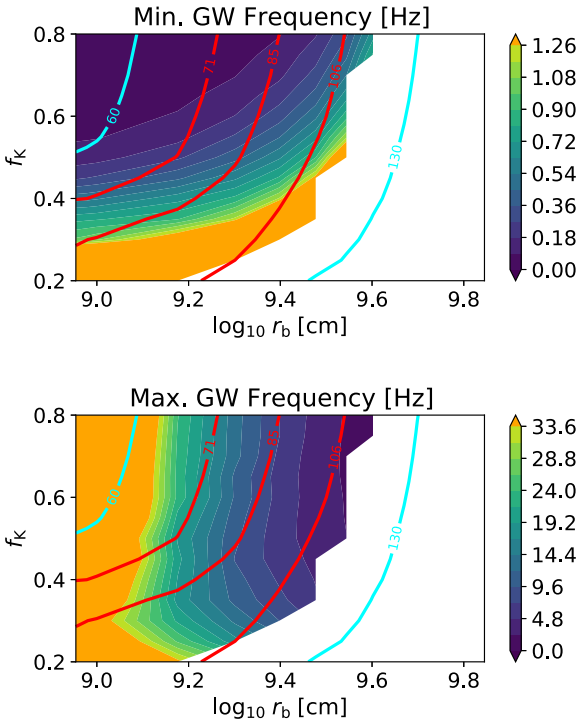

Figure 21. Mininum (top) and maximum (bottom) frequencies of the predicted $l = m = 2$ gravitational-wave emission during the gravitationally unstable phase of collapsar accretion, for the same model shown in Figure 9. The final BH mass contours are drawn as in previous figures.

We characterize the gravitational-wave emission in the frequency domain (positive frequencies f only), by computing the characteristic strain, defined as

$$h_c = 2f|\tilde{h}^{\rm res}(f)|. \tag{F3}$$

For an estimate of the horizon distance, we assume that the detector receives a signal from a directly overhead source, and hence the optimal strain response at the detector can be written as

$$\tilde{h}^{\rm res} = \sqrt{|\tilde{h}_+|^2 + |\tilde{h}_\times|^2}, \tag{F4}$$

where $\tilde{h}_+$ and $\tilde{h}_\times$ are the Fourier transforms of the respective polarization strain amplitudes that we compute, employing a Tukey window function that is limited to the physical frequencies between the maximum and minimum frequencies expected from disk evolution (Figure 21). We compare the gravitational-wave signals to the detector sensitivity in terms of the amplitude spectral density $\sqrt{S_h}$ (Moore et al. 2015):

$$\sqrt{S_h} = 2\sqrt{f}\,|\tilde{h}^{\rm res}|, \tag{F5}$$

where S_h denotes the power spectral density, and we calculate the S/N using an optimal filter (Moore et al. 2015):

$$\mathrm{S/N} = \left(\int df \frac{h_c^2}{S_n f^2}\right)^{\frac{1}{2}}. \tag{F6}$$

The characteristic strains of superKN collapsars range from $\sim 10^{-24}$ to 10^{-22}, depending on the rotation profile of the progenitor. A representative example is shown in Figure 22. Detection horizons for aLIGO and BBO, assuming S/N = 8, are shown in Figure 23, while those for CE, ET, and DECIGO are presented in Figure 13.

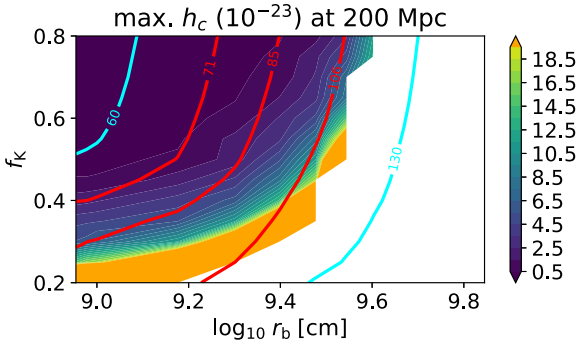

Figure 22. The maximum strain amplitude of the characteristic strain h_c of the gravitational waves from nonaxisymmetric instabilities in self-gravitating collapsar disks across the parameter space of $\{r_b, f_K\}$ for our fiducial model shown in Figure 2, with $p = 4.5$, $f_K = 0.3$, and $r_b = 1.5 \times 10^9$ cm. The characteristic strains range from $\sim 10^{-24}$ to 10^{-22}, depending on the rotation profile of the progenitor. The final BH mass contours are drawn as in previous figures.

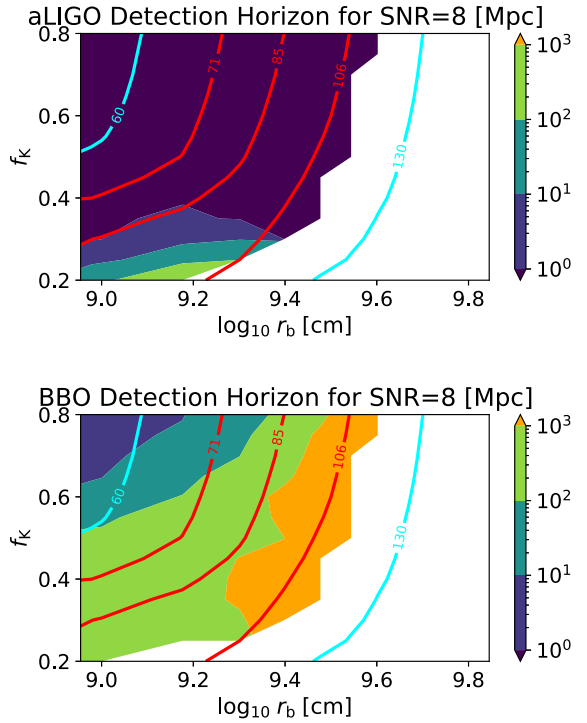

Figure 23. Detection horizons for the gravitational waves from our fiducial model shown in Figure 2, with $p = 4.5$, $f_K = 0.3$, and $r_b = 1.5 \times 10^9$ cm, for aLIGO at design sensitivity (top) and BBO (bottom), assuming optimal matched filtering and an S/N of 8. While the detection horizon for aLIGO is typically limited to $\lesssim$100 Mpc, BBO will typically be able to detect such sources from up to several hundred Mpc to several Gpc, with particular sensitivity to progenitors with low–angular momentum "cores" (medium to large values of r_b). The contours delineate the final BH masses, as in previous figures.

ORCID iDs

Daniel M. Siegel https://orcid.org/0000-0001-6374-6465
Aman Agarwal https://orcid.org/0000-0002-8685-5477
Jennifer Barnes https://orcid.org/0000-0003-3340-4784
Brian D. Metzger https://orcid.org/0000-0002-4670-7509
Mathieu Renzo https://orcid.org/0000-0002-6718-9472
V. Ashley Villar https://orcid.org/0000-0002-5814-4061

References

Abbott, R., Abbott, T. D., Abbott, S., et al. 2020, PhRvL, 125, 101102
Antonini, F., & Rasio, F. A. 2016, ApJ, 831, 187
Aoki, W., Tominaga, N., Beers, T. C., Honda, S., & Lee, Y. S. 2014, Sci, 345, 912
Arnett, W. D. 1982, ApJ, 253, 785
Arnould, M., Goriely, S., & Takahashi, K. 2007, PhR, 450, 97
Bardeen, J. M., Press, W. H., & Teukolsky, S. A. 1972, ApJ, 178, 347
Barnes, J., Duffell, P. C., Liu, Y., et al. 2018, ApJ, 860, 38
Barnes, J., & Kasen, D. 2013, ApJ, 775, 18
Barnes, J., Kasen, D., Wu, M.-R., & Martínez-Pinedo, G. 2016, ApJ, 829, 110
Barnes, J., & Metzger, B. D. 2022, ApJL, 939, L29
Barnes, J., Zhu, Y. L., Lund, K. A., et al. 2021, ApJ, 918, 44
Bartos, I., & Márka, S. 2019, ApJL, 881, L4
Belczynski, K., Holz, D. E., Bulik, T., & O'Shaughnessy, R. 2016, Natur, 534, 512
Beloborodov, A. M. 2003, ApJ, 588, 931
Berger, E. 2014, ARA&A, 52, 43
Blandford, R. D., & Begelman, M. C. 1999, MNRAS, 303, L1
Bond, J. R., Arnett, W. D., & Carr, B. J. 1984, ApJ, 280, 825
Bose, S., Valenti, S., Misra, K., et al. 2015, MNRAS, 450, 2373
Brauer, K., Ji, A. P., Drout, M. R., & Frebel, A. 2021, ApJ, 915, 81
Bromberg, O., Nakar, E., Piran, T., & Sari, R. 2012, ApJ, 749, 110
Burbidge, E. M., Burbidge, G. R., Fowler, W. A., & Hoyle, F. 1957, RvMP, 29, 547
Cain, M., Frebel, A., Ji, A. P., et al. 2020, ApJ, 898, 40
Callister, T. A., Farr, W. M., & Renzo, M. 2021, ApJ, 920, 157
Cameron, A. G. W. 1957, PASP, 69, 201
Cano, Z. 2016, in Eighth Huntsville Gamma-Ray Burst Symp. No. 1962 (Huntsville, AL: LPI), 4116
Cano, Z., Johansson Andreas, K. G., & Maeda, K. 2016, MNRAS, 457, 2761
Cantiello, M., Jermyn, A. S., & Lin, D. N. C. 2021, ApJ, 910, 94
Chen, W.-X., & Beloborodov, A. M. 2007, ApJ, 657, 383
Christie, I. M., Lalakos, A., Tchekhovskoy, A., et al. 2019, MNRAS, 490, 4811
Costa, G., Bressan, A., Mapelli, M., et al. 2021, MNRAS, 501, 4514
Côté, B., Eichler, M., Arcones, A., et al. 2019, ApJ, 875, 106
Cowan, J. J., Sneden, C., Lawler, J. E., et al. 2021, RvMP, 93, 015002
Cowperthwaite, P., Berger, E., Villar, V., et al. 2017, ApJL, 848, L17
Crowther, P. A., Caballero-Nieves, S. M., Bostroem, K. A., et al. 2016, MNRAS, 458, 624
de Koter, A., Heap, S. R., & Hubeny, I. 1997, ApJ, 477, 792
de Mink, S. E., & Mandel, I. 2016, MNRAS, 460, 3545
De, S., & Siegel, D. 2020, arXiv:2011.07176
Delgado, F., & Reuter, M. A. 2016, Proc. SPIE, 9910, 991013
Dessart, L., Burrows, A., Livne, E., & Ott, C. D. 2008, ApJL, 673, L43
Di Carlo, U. N., Giacobbo, N., Mapelli, M., et al. 2019, MNRAS, 487, 2947
Di Carlo, U. N., Mapelli, M., Giacobbo, N., et al. 2020, MNRAS, 498, 495
Di Matteo, T., Perna, R., & Narayan, R. 2002, ApJ, 579, 706
Dittmann, A. J., Cantiello, M., & Jermyn, A. S. 2021, ApJ, 916, 48
Drout, M., Piro, A., Shappee, B., et al. 2017, Sci, 358, 1570
Duggan, G. E., Kirby, E. N., Andrievsky, S. M., & Korotin, S. A. 2018, ApJ, 869, 50
Eftekhari, T., Berger, E., Margalit, B., Metzger, B. D., & Williams, P. K. G. 2020, ApJ, 895, 98
Farmer, R., Fields, C. E., Petermann, I., et al. 2016, ApJS, 227, 22
Farmer, R., Renzo, M., de Mink, S. E., Fishbach, M., & Justham, S. 2020, ApJL, 902, L36
Farmer, R., Renzo, M., de Mink, S. E., Marchant, P., & Justham, S. 2019, ApJ, 887, 53
Farrell, E., Groh, J. H., Hirschi, R., et al. 2021, MNRAS, 502, L40
Fernández, R., Kasen, D., Metzger, B. D., & Quataert, E. 2015, MNRAS, 446, 750
Fernández, R., & Metzger, B. D. 2013, MNRAS, 435, 502
Fernández, R., Tchekhovskoy, A., Quataert, E., Foucart, F., & Kasen, D. 2019, MNRAS, 482, 3373
Fishbach, M., & Holz, D. E. 2020, ApJL, 904, L26
Fruchter, A. S., Levan, A. J., Strolger, L., et al. 2006, Natur, 441, 463
Fujibayashi, S., Kiuchi, K., Nishimura, N., Sekiguchi, Y., & Shibata, M. 2018, ApJ, 860, 64
Fujibayashi, S., Shibata, M., Wanajo, S., et al. 2020, PhRvD, 101, 083029
Fujibayashi, S., Takahashi, K., Sekiguchi, Y., & Shibata, M. 2021, ApJ, 919, 80
Fuller, J., & Ma, L. 2019, ApJL, 881, L1
Fynbo, J. P. U., Watson, D., Thöne, C. C., et al. 2006, Natur, 444, 1047

Gall, C., Hjorth, J., Rosswog, S., Tanvir, N. R., & Levan, A. J. 2017, ApJL, 849, L19
Gammie, C. F. 2001, ApJ, 553, 174
Gehrels, N., Norris, J. P., Barthelmy, S. D., et al. 2006, Natur, 444, 1044
Gerosa, D., & Fishbach, M. 2021, NatAs, 5, 749
Glatzel, W., Fricke, K. J., & El Eid, M. F. 1985, A&A, 149, 413
Goldstein, A., Connaughton, V., Briggs, M. S., & Burns, E. 2016, ApJ, 818, 18
Gottlieb, O., Lalakos, A., Bromberg, O., Liska, M., & Tchekhovskoy, A. 2021, arXiv:2109.14619
Graham, M. J., Ford, K. E. S., McKernan, B., et al. 2020, PhRvL, 124, 251102
Grichener, A., & Soker, N. 2019, ApJ, 878, 24
Heger, A., Langer, N., & Woosley, S. E. 2000, ApJ, 528, 368
Hiramatsu, D., Howell, D. A., Van Dyk, S. D., et al. 2021, NatAs, 5, 903
Holmbeck, E. M., Frebel, A., McLaughlin, G. C., et al. 2019, ApJ, 881, 5
Horowitz, C. J., Arcones, A., Côté, B., et al. 2019, JPhG, 46, 083001
Hotokezaka, K., Piran, T., & Paul, M. 2015, NatPh, 11, 1042
Hotokezaka, K., Tanaka, M., Kato, D., & Gaigalas, G. 2021, MNRAS, 506, 5863
Janiuk, A., Perna, R., Di Matteo, T., & Czerny, B. 2004, MNRAS, 355, 950
Japelj, J., Vergani, S. D., Salvaterra, R., et al. 2018, A&A, 617, A105
Jermyn, A. S., Dittmann, A. J., Cantiello, M., & Perna, R. 2021, ApJ, 914, 105
Ji, A. P., Frebel, A., Chiti, A., & Simon, J. D. 2016, Natur, 531, 610
Jin, Z.-P., Li, X., Cano, Z., et al. 2015, ApJL, 811, L22
Just, O., Bauswein, A., Pulpillo, R. A., Goriely, S., & Janka, H.-T. 2015, MNRAS, 448, 541
Just, O., Goriely, S., Janka, H.-T., Nagataki, S., & Bauswein, A. 2022, MNRAS, 509, 1377
Kalogera, V. 1996, ApJ, 471, 352
Kasen, D., Badnell, N. R., & Barnes, J. 2013, ApJ, 774, 25
Kasen, D., Thomas, R. C., & Nugent, P. 2006, ApJ, 651, 366
Kasliwal, M. M., Bally, J., et al. 2017, ApJ, 839, 88
Khatami, D. K., & Kasen, D. N. 2019, ApJ, 878, 56
Kiuchi, K., Yoshida, S., & Shibata, M. 2011, A&A, 532, A30
Kumar, P., Narayan, R., & Johnson, J. L. 2008, MNRAS, 388, 1729
Langer, N. 1998, A&A, 329, 551
Lattimer, J. M., & Schramm, D. N. 1974, ApJL, 192, L145
Li, L.-X., & Paczyński, B. 1998, ApJL, 507, L59
Li, X., & Siegel, D. M. 2021, PhRvL, 126, 251101
Liang, E., Zhang, B., Virgili, F., & Dai, Z. G. 2007, ApJ, 662, 1111
Lippuner, J., & Roberts, L. F. 2015, ApJ, 815, 82
Ma, L., & Fuller, J. 2019, MNRAS, 488, 4338
MacFadyen, A. I., & Woosley, S. E. 1999, ApJ, 524, 262
Macias, P., & Ramirez-Ruiz, E. 2019, ApJL, 877, L24
Maeder, A., & Meynet, G. 2000, ARA&A, 38, 143
Mandel, I., & de Mink, S. E. 2016, MNRAS, 458, 2634
Mandel, I., & Fragos, T. 2020, ApJL, 895, L28
Marchant, P., Langer, N., Podsiadlowski, P., Tauris, T. M., & Moriya, T. J. 2016, A&A, 588, A50
Marchant, P., & Moriya, T. J. 2020, A&A, 640, L18
Marchant, P., Renzo, M., Farmer, R., et al. 2019, ApJ, 882, 36
Margutti, R., & Chornock, R. 2021, ARA&A, 59, 155
McMillan, P. J. 2017, MNRAS, 465, 76
Mehta, A. K., Buonanno, A., Gair, J., et al. 2022, ApJ, 924, 39
Metzger, B. D. 2019, LRR, 23, 1
Metzger, B. D., & Bower, G. C. 2014, MNRAS, 437, 1821
Metzger, B. D., Martínez-Pinedo, G., Darbha, S., et al. 2010, MNRAS, 406, 2650
Metzger, B. D., Piro, A. L., & Quataert, E. 2008, MNRAS, 390, 781
Metzger, B. D., Thompson, T. A., & Quataert, E. 2007, ApJ, 659, 561
Metzger, B. D., Thompson, T. A., & Quataert, E. 2008, ApJ, 676, 1130
Metzger, B. D., Williams, P. K. G., & Berger, E. 2015, ApJ, 806, 224
Miller, J. M., Sprouse, T. M., Fryer, C. L., et al. 2020, ApJ, 902, 66
Modjaz, M., Bianco, F. B., Siwek, M., et al. 2020, ApJ, 892, 153
Moore, C. J., Cole, R. H., & Berry, C. P. L. 2015, CQGra , 32, 015014
Nakar, E. 2020, PhR, 886, 1
Nakar, E., & Piran, T. 2011, Natur, 478, 82
Narayana Bhat, P., Meegan, C. A., von Kienlin, A., et al. 2016, ApJS, 223, 28
Nishimura, N., Takiwaki, T., & Thielemann, F.-K. 2015, ApJ, 810, 109
Nitz, A. H., & Capano, C. D. 2021, ApJL, 907, L9
Ofek, E. O. 2017, ApJ, 846, 44
Paczynski, B. 1978, AcA, 28, 91
Pedregosa, F., Varoquaux, G., Gramfort, A., et al. 2011, J. Mach. Learn. Res., 12, 2825
Perna, R., Lazzati, D., & Cantiello, M. 2021, ApJL, 906, L7
Pescalli, A., Ghirlanda, G., Salvaterra, R., et al. 2016, A&A, 587, A40
Petrosian, V., Kitanidis, E., & Kocevski, D. 2015, ApJ, 806, 44
Powell, J., Müller, B., & Heger, A. 2021, MNRAS, 503, 2108
Qian, Y.-Z., & Woosley, S. E. 1996, ApJ, 471, 331
Rastinejad, J. C., Gompertz, B. P., Levan, A. J., et al. 2022, arXiv:2204.10864
Raynaud, R., Guilet, J., Janka, H.-T., & Gastine, T. 2020, SciA, 6, eaay2732
Renzo, M., Cantiello, M., Metzger, B. D., & Jiang, Y. F. 2020a, ApJL, 904, L13
Renzo, M., Farmer, R., Justham, S., et al. 2020b, A&A, 640, A56
Roberts, L. F., Woosley, S. E., & Hoffman, R. D. 2010, ApJ, 722, 954
Safarzadeh, M., & Haiman, Z. 2020, ApJL, 903, L21
Schlegel, D. J., Finkbeiner, D. P., & Davis, M. 1998, ApJ, 500, 525
Schneider, F. R. N., Sana, H., Evans, C. J., et al. 2018, Sci, 359, 69
Schroeder, G., Margalit, B., Fong, W.-F., et al. 2020, ApJ, 902, 82
Shakura, N. I., & Sunyaev, R. A. 1973, A&A, 24, 337
Shankar, S., Mösta, P., Barnes, J., Duffell, P. C., & Kasen, D. 2021, MNRAS, 508, 5390
Shapiro, S. L., & Teukolsky, S. A. 1983, Black Holes, White Dwarfs, and Neutron Stars (New York: Wiley)
Shen, S., Cooke, R. J., Ramirez-Ruiz, E., et al. 2015, ApJ, 807, 115
Shibata, M., Kiuchi, K., Fujibayashi, S., & Sekiguchi, Y. 2021, PhRvD, 103, 063037
Siegel, D. M. 2019, EPJA, 55, 203
Siegel, D. M. 2022, NatRP, 4, 306
Siegel, D. M., Barnes, J., & Metzger, B. D. 2019, Natur, 569, 241
Siegel, D. M., & Metzger, B. D. 2017, PhRvL, 119, 231102
Siegel, D. M., & Metzger, B. D. 2018, ApJ, 858, 52
Smith, N., Li, W., Foley, R. J., et al. 2007, ApJ, 666, 1116
Sobacchi, E., Granot, J., Bromberg, O., & Sormani, M. C. 2017, MNRAS, 472, 616
Spergel, D., Gehrels, N., Baltay, C., et al. 2015, arXiv:1503.03757
Spruit, H. C. 2002, A&A, 381, 923
Sun, H., Zhang, B., & Li, Z. 2015, ApJ, 812, 33
Surman, R., McLaughlin, G. C., & Hix, W. R. 2006, ApJ, 643, 1057
Surman, R., McLaughlin, G. C., Ruffert, M., Janka, H.-T., & Hix, W. R. 2008, ApJL, 679, L117
Symbalisty, E., & Schramm, D. N. 1982, ApL, 22, 143
Tagawa, H., Haiman, Z., Bartos, I., Kocsis, B., & Omukai, K. 2021, MNRAS, 507, 3362
Takami, H., Nozawa, T., & Ioka, K. 2014, ApJL, 789, L6
Tanaka, M., & Hotokezaka, K. 2013, ApJ, 775, 113
Tanaka, M., Kato, D., Gaigalas, G., & Kawaguchi, K. 2020, MNRAS, 496, 1369
Tarumi, Y., Hotokezaka, K., & Beniamini, P. 2021, ApJL, 913, L30
The LIGO Scientific Collaboration, the Virgo Collaboration, the KAGRA Collaboration 2021, arXiv:2111.03634
Thompson, C., & Duncan, R. C. 1993, ApJ, 408, 194
Thompson, T. A., Chang, P., & Quataert, E. 2004, ApJ, 611, 380
Tomita, H., Deng, J., Maeda, K., et al. 2006, ApJ, 644, 400
Tsujimoto, T., Matsuno, T., Aoki, W., Ishigaki, M. N., & Shigeyama, T. 2017, ApJL, 850, L12
Tsvetkov, D. Y., Shugarov, S. Y., Volkov, I. M., et al. 2013, CoSka, 43, 94
Tyson, J. A. 2002, Proc. SPIE, 4836, 10
van de Voort, F., Pakmor, R., Grand, R. J. J., et al. 2020, MNRAS, 494, 4867
van den Heuvel, E. P. J., Portegies Zwart, S. F., & de Mink, S. E. 2017, MNRAS, 471, 4256
van Son, L. A. C., de Mink, S. E., Callister, T., et al. 2022, ApJ, 931, 17
Villar, V. A., Guillochon, J., Berger, E., et al. 2017, ApJL, 851, L21
Vink, J. S., Higgins, E. R., Sander, A. A. C., & Sabhahit, G. N. 2021, MNRAS, 504, 146
Wallner, A., Faestermann, T., Feige, J., et al. 2015, NatCo, 6, 5956
Wanderman, D., & Piran, T. 2010, MNRAS, 406, 1944
Wessel, E., Paschalidis, V., Tsokaros, A., Ruiz, M., & Shapiro, S. L. 2021, PhRvD, 103, 043013
Winteler, C., Käppeli, R., Perego, A., et al. 2012, ApJL, 750, L22
Woosley, S. E. 2017, ApJ, 836, 244
Woosley, S. E., & Bloom, J. S. 2006, ARA&A, 44, 507
Woosley, S. E., & Heger, A. 2006, ApJ, 637, 914
Woosley, S. E., & Heger, A. 2021, ApJL, 912, L31
Woosley, S. E., Heger, A., & Weaver, T. A. 2002, RvMP, 74, 1015
Woosley, S. E., & Hoffman, R. D. 1992, ApJ, 395, 202
Yagi, K., & Seto, N. 2011, PhRvD, 83, 044011
Yamazaki, Y., Kajino, T., Mathews, G. J., et al. 2021, arXiv:2102.05891
Yang, Y., Bartos, I., Gayathri, V., et al. 2019, PhRvL, 123, 181101
Yüksel, H., Kistler, M. D., Beacom, J. F., & Hopkins, A. M. 2008, ApJL, 683, L5
Zenati, Y., Siegel, D. M., Metzger, B. D., & Perets, H. B. 2020, MNRAS, 499, 4097
Zhang, B., Zhang, B.-B., Liang, E.-W., et al. 2007, ApJL, 655, L25